European Journal of Mechanics / A Solids 113 (2025) 105713

Contents lists available at ScienceDirect

European Journal of Mechanics / A Solids

journal homepage: www.elsevier.com/locate/ejmsol

Full length article

Multiphysics modeling of surface diffusion coupled with large deformation in 3D solids

Seung-Hwan Boo [a], Jaemin Kim [b,*]

[a] Division of Naval Architecture and Ocean Systems Engineering, Korea Maritime and Ocean University, Busan 49112, Republic of Korea
[b] Department of Mechanical Engineering, Changwon National University, Changwon 51140, Republic of Korea

ARTICLE INFO

Keywords:
Film
Substrate
Surface diffusion
Viscoelasticity
Non-equilibrium
Indentation
Multiphysics

ABSTRACT

This study presents a comprehensive theoretical and computational model that explores the behavior of a thin hydrated film bonded to a non-hydrated/impermeable soft substrate in the context of surface and bulk elasticity coupled with surface diffusion kinetics. This type of coupling manifests as an integral aspect in diverse engineering processes encountered in optical interference coatings, tissue engineering, soft electronics, and can prove important in the design process for the next generation of sensors and actuators, especially as the focus is shifted to systems in smaller length scales. The intricate interplay between solvent diffusion and deformation of the film is governed by surface poroelasticity, and the viscoelastic deformation of the substrate. While existing methodologies offer tools for studying coupled poroelasticity involving solvent diffusion and network deformation, there exists a gap in understanding how coupled poroelastic processes occurring in a film attached to the boundary of a highly deformable solid can influence its response. In this study, we introduce a non-equilibrium thermodynamics formulation encompassing the multiphysical processes of surface poroelasticity and bulk viscoelasticity, complemented by a corresponding finite element implementation. This study makes significant contributions to solid mechanics and computational modeling by (i) modeling surface diffusion coupled with a viscoelastic substrate, enabling the study of time-dependent responses critical for practical applications, (ii) providing a robust theoretical framework for coupling two materials (film and substrate) with distinct reference (stress-free) states, including a detailed analytical derivation of the initial state, and (iii) efficiently modeling the thin film using a 2D mesh to avoid the need for a fine 3D solid mesh, thus reducing computational costs while maintaining accuracy. This work contributes valuable insights, particularly in scenarios where the coupling of surface diffusion kinetics and substrate elasticity is an important design factor.

1. Introduction

The field of soft solid mechanics has attracted significant attention due to its diverse range of potential applications, spanning from the design of biocompatible materials (Lin et al., 2016; Yang et al., 2020) to investigations in mechanobiology (Baker et al., 2015; Hall et al., 2016; Kim et al., 2020, 2023a, 2024) and tissue engineering (Mailand et al., 2022; Rossy et al., 2023). Additionally, it extends to advancements in soft robotics (Martinez et al., 2014; Wallin et al., 2018), flexible electronics (Hu et al., 2023; Fu et al., 2023), wearable electronics (Liu and Wang, 2020), microfluidic device fabrication (Cheng et al., 2007; Kopecek, 2009), and the development of drug delivery systems (Stamatialis et al., 2008; Park et al., 2017; Chen et al., 2020). In these applications, the hydrogels and porous polymeric films are often used for coating the substrate (Wiener et al., 2014; Delavoipière et al., 2018; Moreau et al., 2016; Huo et al., 2022), and the interaction of films with soft substrates is pivotal. Here, the deformation of these substrate materials plays a fundamental role in determining the dynamic response of coated soft solids (Lucantonio et al., 2016; Song et al., 2020, 2023). For instance, surface instabilities arise due to confinement during swelling or externally applied compressive stresses (Toomey et al., 2004; Li et al., 2012; Liu et al., 2024). A similar thin-film/substrate setup is also widely adopted in the study of mechanobiology, where cell migration and formation of epithelial sheets can occur on soft solid substrates (Reinhart-King et al., 2005; Tse and Engler, 2010; Rens and Merks, 2020). Therefore, understanding the transient responses of multiphysical surface processes occurring on highly-deforming soft solid substrates is imperative for ensuring improved predictive capabilities for these diverse applications (Xu et al., 2020; Björklund et al., 2024). In continuum thermodynamics, the non-equilibrium processes are often

* Corresponding author.
E-mail address: jaeminkim@changwon.ac.kr (J. Kim).

https://doi.org/10.1016/j.euromechsol.2025.105713
Received 14 October 2024; Received in revised form 6 April 2025; Accepted 5 May 2025
Available online 19 May 2025

modeled with internal variables, capturing time-dependent mechanical behaviors, such as relaxation and diffusion (Holzapfel, 2002; Song et al., 2023).

Motivated by applications in diverse and emerging fields, we investigate a hydrogel film experiencing solvent diffusion during the deformation of a three-dimensional (3D) soft but impermeable substrate to which it is rigidly bonded. Building upon prior works (Steinmann, 2008; Javili and Steinmann, 2009, 2010; McBride et al., 2011; Lucantonio et al., 2016; Goodbrake and Steigmann, 2018; Dortdivanlioglu and Javili, 2021; Kim et al., 2023b), we model the film in the context of surface poroelasticity. As the substrate is deformed the solvent concentration in the film can change depending on the location on the surface and deformation history at that point. Notably, considering that the film is tethered to the substrate surface, we describe it as a two-dimensional (2D) structure. This work is also relevant to cases where an impermeable polymer body has a functionalized hydrophilic surface, enabling surface diffusion upon deformation of the bulk, and surface elasticity also becomes important as one moves to smaller length scales (Drelich et al., 2011; Rasitha et al., 2024). While earlier studies laid the theoretical groundwork, finite element implementation that considers surface poroelasticity and bulk viscoelasticity (for the substrate) becomes crucial to fully understand these coupled phenomena in the multiphysics framework.

An extensive body of work has focused on the development of nonlinear poroelastic theories for gels (Hong et al., 2008; Chester and Anand, 2010), and corresponding mixed finite element frameworks (Lucantonio et al., 2013; Chester et al., 2015; MacMinn et al., 2016; Xue et al., 2024; Xu and Liu, 2023, 2020; Askari-Sedeh and Baghani, 2023; Liu et al., 2023), ensuring satisfaction of the Ladyzhenskaya–Babuška–Brezzi (LBB) condition (Babuška, 1971; Brezzi, 1974; Murad and Loula, 1994; Bathe, 2001). Existing frameworks (Javili and Steinmann, 2009, 2010) address finite deformation with surface elasticity, and subsequent extensions (McBride et al., 2011; Steinmann et al., 2012) encompass various coupled problems. Several recent works have also followed into this topic coupling poroelasticity with surface processes (Ang et al., 2020; Kim et al., 2023b,a). However, considering the poroelastic behavior of a film on a deforming substrate is non-trivial because the wet film is initially not stress-free, and the stress-free reference state of the film is obtained in its dry condition. Thus, establishing the initial state of composite solids consisting of a swollen film and a finitely deforming substrate presents a significant challenge. To the best of the authors' knowledge, the proposed model is the first attempt to couple diffusion within a film and the deformation of a substrate in continuum mechanics framework and finite element simulation. Taken together, the present work makes significant contributions to the solid mechanics and computational modeling in the following ways: (i) It models surface diffusion coupled with a viscoelastic substrate, enabling the study of time-dependent responses—a critical aspect for many practical applications. (ii) It offers a robust theoretical framework for coupling two materials (film and substrate) with distinct reference (stress-free) states, including a detailed analytical derivation of the initial state. (iii) The thin film is efficiently modeled using a 2D surface mesh to avoid the computational cost of employing a fine 3D solid mesh. Specifically, while the diffusion within the poroelastic film is modeled physically, the film is represented computationally as a 2D surface mesh embedded on a 3D solid mesh. This approach reduces computational costs while maintaining accuracy, making the method suitable for large-scale, practical simulations.

Our study unveils multiphysical complexities not typically addressed in the previous studies. This complexity arises from the intricate coupling of surface poroelasticity and bulk viscoelasticity. The validity of our theoretical predictions is established through three distinct numerical experiments, offering valuable insights into both viscoelastic and poroelastic relaxation driven by bulk, and surface mechanisms. The manuscript is organized as follows: In Section 2, we describe the coupled theory, encompassing kinematics, balance laws, and the general form of constitutive equations considering both bulk and surface energetics. In Section 3, we specialize the free energies for a poroelastic hydrogel film and a viscoelastic substrate. Section 4 details the finite element implementation, including the weak form, normalization, and solution procedure. Section 5 elaborates the numerical simulations for three boundary value problems: (i) uniaxial tension of a cylindrical bar highlighting the effect of a tension-driven deformation of a substrate, (ii) response under bending showcasing the competing contributions of compression and tension along with competing surface diffusion pathways, and (iii) a rigid sphere indentation of a film/substrate system. Finally, Section 6 provides conclusions and outlines the future research directions.

Remark 1 (*Notation*)**.** The following notations and conventions are used throughout the text:

1. The dyad ($\otimes$) and dot ($\cdot$) denote the tensor and dot products, respectively.
2. The double dot ($:$) denotes the double contraction over two second-order tensors, e.g., $\mathbf{A} : \mathbf{B} = A_{ij}B_{ij}$.
3. We adopt the Einstein summation convention, where repeated indices imply summation over all values of the index.
4. Latin indices (e.g., i, j) take the values 1, 2, 3 and are used in the context of variables describing the three-dimensional Euclidean space.
5. Greek indices (e.g., α, β) take the values 1, 2 and are used for variables embedded in the two-dimensional surface.
6. Bulk quantities are denoted by symbols without a tilde (e.g., $\mathbf{A}$), while surface quantities are denoted with an over-tilde (e.g., $\widetilde{\mathbf{A}}$) for a body occupying volume V and bounded by outer surface S
7. The superposed dot (e.g., $\dot{\mathbf{A}}$) represents the material time derivative, and superposed check (e.g., $\check{\mathbf{A}}$) denotes the prescribed boundary condition.
8. For tensor operations:
   (a) $\mathbf{A}^{-1}$ denotes the inverse of tensor $\mathbf{A}$,
   (b) $\mathrm{tr}\,(\mathbf{A})$ is the trace of $\mathbf{A}$,
   (c) $\det(\mathbf{A})$ and $\mathrm{cof}\,(\mathbf{A})$ represent the determinant and cofactor of tensor $\mathbf{A}$, respectively.
9. The double-bracket notation ($[[\widetilde{\mathbf{A}}]]$) is used to represent the average and jump of a surface quantity ($\widetilde{\mathbf{A}}$) over an interface $C_k := \partial S_k$

$$[[\widetilde{\mathbf{W}} \cdot \widetilde{\mathbf{N}}]] = \widetilde{\mathbf{W}}_+ \cdot \widetilde{\mathbf{N}}_+ + \widetilde{\mathbf{W}}_- \cdot \widetilde{\mathbf{N}}_- = \left(\widetilde{\mathbf{W}}_+ - \widetilde{\mathbf{W}}_-\right) \cdot \widetilde{\mathbf{N}}_+ = \sum_{C_k} \widetilde{\mathbf{W}} \cdot \widetilde{\mathbf{N}}$$

where the subscripts $\{\widetilde{\bullet}\}_+$ and $\{\widetilde{\bullet}\}_-$ denote the surface quantity on the outward and inward of the interface, respectively, and we define the surface outward normal vector $\widetilde{\mathbf{N}} := \widetilde{\mathbf{N}}_+$ over the interface C_k.

2. A coupled continuum theory for non-equilibrium processes

2.1. Kinematics

We use the notation $\varphi : (V, t) \to \upsilon$ for the deformation of body $\mathcal{B}$, where the continuum body $\mathcal{B}$ moves in space from one instant of time to another denoted by initial state V and current state υ (Fig. 1). A motion φ is the vector field of the mapping $\boldsymbol{x} = \varphi(\mathbf{X}, t)$, of a material point in the reference configuration $\mathbf{X} \in V$ to a position in the deformed configuration $\boldsymbol{x} \in \upsilon$. The kinematics of a typical particle are described by the displacement vector field in the spatial description, $\mathbf{u}(\mathbf{X}, t) = \boldsymbol{x}(\mathbf{X}, t) - \mathbf{X}$. The kinematics of an infinitesimal bulk element are described by

$$\mathbf{F}(\mathbf{X}, t) = \frac{\partial \varphi(\mathbf{X}, t)}{\partial \mathbf{X}} = \boldsymbol{\nabla}_{\mathbf{X}}\, \varphi(\mathbf{X}, t) \tag{2.1}$$

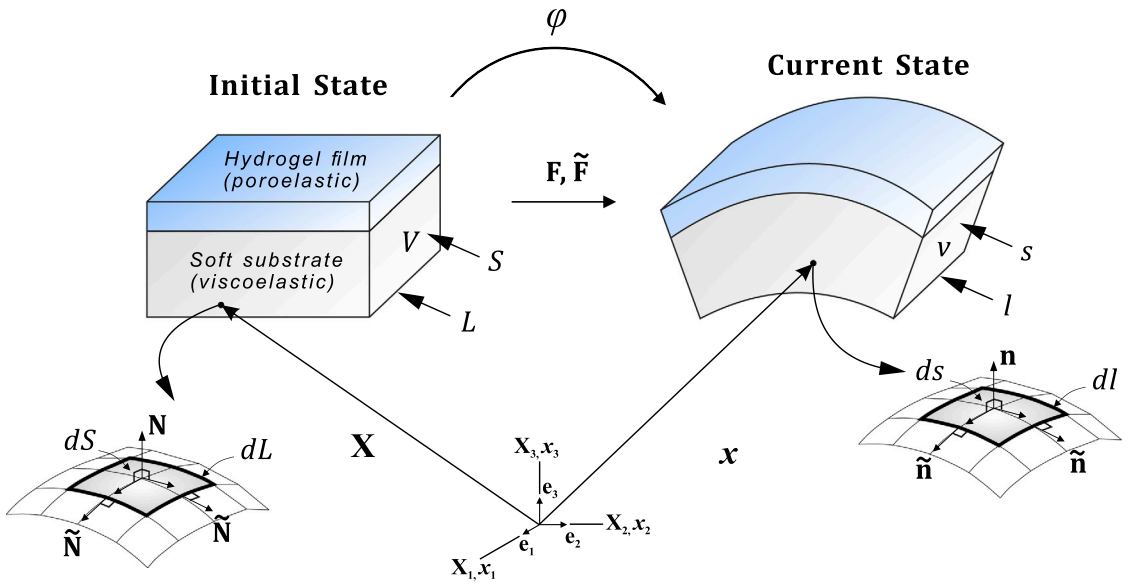

Fig. 1. Schematic illustration of the initial and current states of a continuum body. The bulk and surface deformation gradients are denoted by $\mathbf{F}$ and $\widetilde{\mathbf{F}}$, respectively. The initial volume and surface, and boundary are denoted by V and S, and L respectively. The current volume and surface, and boundary are denoted by v and s, and l respectively. The normal vector to the surface in the reference and current configuration ($\mathbf{N}$ and $\mathbf{n}$) and the bi-normal vector to the boundary ($\widetilde{\mathbf{N}}$ and $\widetilde{\mathbf{n}}$) are shown, where the over-tilde indicates surface quantities. Note that we assume the hydrogel film is in a fully swollen state, which is not stress-free. To define the initial stress state, we establish a reference state corresponding to the fully dry, stress-free configuration (see Appendix A).

$$\mathbf{F}^{-1}(\boldsymbol{x},t)=\frac{\partial\varphi^{-1}(\boldsymbol{x},t)}{\partial\boldsymbol{x}}=\boldsymbol{\nabla}_{\boldsymbol{x}}\,\varphi^{-1}(\boldsymbol{x},t) \tag{2.2}$$

where $\mathbf{F}(\mathbf{X},t)$ and $\mathbf{F}^{-1}(\boldsymbol{x},t)$ are the deformation gradient and inverse deformation gradient, respectively. Note that $J(\mathbf{X},t)=\mathrm{d}v/\mathrm{d}V=\det\mathbf{F}(\mathbf{X},t)>0$ is the Jacobian determinant of the deformation gradient defining the ratio of a volume element between the material and spatial configuration. We decompose the deformation gradient into a volumetric and an isochoric part (Flory, 1961; Holzapfel, 2002).

$$\mathbf{F}=(J^{1/3}\mathbf{I})\cdot\overline{\mathbf{F}} \tag{2.3}$$

where $J^{1/3}\,\mathbf{I}$ and $\overline{\mathbf{F}}$ represent the volumetric and isochoric parts of the deformation gradient $\mathbf{F}$, and $\{\,\cdot\,\}$ denotes the dot product. Following, we utilize $\{\,\overline{\bullet}\,\}$ to denote quantities associated with the isochoric part of the deformation.

In the context of displacement conformity on surface, the surface displacement can be determined by $\widetilde{\mathbf{u}}(\widetilde{\mathbf{X}},t)=\mathbf{u}(\mathbf{X},t)|_S$, where $\widetilde{\mathbf{X}}=\mathbf{X}|_S$ is the surface position vector. When describing the motion of an arbitrary infinitesimal vector element $\mathrm{d}\mathbf{X}$, it is mapped by the deformation gradient $\mathbf{F}$ to a vector $\mathrm{d}\mathbf{x}$ in the deformed configuration. However, it is important to note that the transformation of a unit normal vector $\mathbf{N}$ from the material configuration to a unit normal vector $\mathbf{n}$ in the spatial configuration cannot be accomplished using the deformation gradient (Holzapfel, 2002; Steinmann, 2008). This distinction leads us to follow the kinematics of an infinitesimal surface element (Kim et al., 2020, 2023a).

$$\widetilde{\mathbf{F}}(\widetilde{\mathbf{X}},t)=\frac{\partial\varphi(\widetilde{\mathbf{X}},t)}{\partial\widetilde{\mathbf{X}}}\cdot\widetilde{\mathbf{I}}=\widetilde{\boldsymbol{\nabla}}_{\widetilde{\mathbf{X}}}\,\varphi(\widetilde{\mathbf{X}},t) \tag{2.4}$$

$$\widetilde{\mathbf{F}}^{-1}(\widetilde{\boldsymbol{x}},t)=\frac{\partial\varphi^{-1}(\widetilde{\boldsymbol{x}},t)}{\partial\widetilde{\boldsymbol{x}}}\cdot\widetilde{\boldsymbol{i}}=\widetilde{\boldsymbol{\nabla}}_{\widetilde{\boldsymbol{x}}}\,\varphi^{-1}(\widetilde{\boldsymbol{x}},t) \tag{2.5}$$

where $\widetilde{\mathbf{F}}(\widetilde{\mathbf{X}},t)$ and $\widetilde{\mathbf{F}}^{-1}(\widetilde{\boldsymbol{x}},t)$ are the surface deformation gradient and inverse surface deformation gradient, and $\widetilde{\mathbf{I}}=\mathbf{I}-\mathbf{N}\otimes\mathbf{N}$ and $\widetilde{\boldsymbol{i}}=\boldsymbol{i}-\mathbf{n}\otimes\mathbf{n}$ are the mixed surface unit tensors with the outward unit normal vectors $\mathbf{N}$ and $\mathbf{n}$. Note that $\widetilde{\mathbf{I}}$ and $\widetilde{\boldsymbol{i}}$ serve as surface (idempotent) projection tensors in the material and spatial configurations, respectively. Furthermore, $\widetilde{\mathbf{F}}$ represents a mapping from the bulk (3D) to the surface (2D), resulting in a rank-deficient tensor. Additionally, $\widetilde{J}(\widetilde{\mathbf{X}},t)=\mathrm{d}a/\mathrm{d}A=|\mathrm{cof}\left(\mathbf{F}(\widetilde{\mathbf{X}},t)\cdot\mathbf{N}\right)|>0$ denotes the Jacobian determinant of the surface deformation gradient. This determinant defines the area ratio of a surface element between the material and spatial configurations. We introduce $\mathbf{C}$ and $\widetilde{\mathbf{C}}$, the right Cauchy–Green tensors in the bulk and on the surface, respectively, as

$$\mathbf{C}=\mathbf{F}^{\mathrm{T}}\cdot\mathbf{F} \tag{2.6}$$

$$\widetilde{\mathbf{C}}=\widetilde{\mathbf{F}}^{\mathrm{T}}\cdot\widetilde{\mathbf{F}} \tag{2.7}$$

and $I_1=\mathrm{tr}(\mathbf{C})$ is the first principal invariant. The detailed derivation for the surface kinematics can be found in the Refs. (Green and Zerna, 1992; Steinmann, 2008; Do Carmo, 2016). Note that we cannot perform the inverse of the surface right Cauchy–Green tensor due to its rank deficiency. Nevertheless, we can still obtain its inverse form in the generalized sense,

$$\widetilde{\mathbf{C}}^{-1}=\widetilde{\mathbf{I}}\cdot\mathbf{C}^{-1}\cdot\widetilde{\mathbf{I}} \tag{2.8}$$

which will play a crucial role in our forthcoming developments as it will be utilized to define the surface kinetic law.

2.2. Mechanical equilibrium

Mechanical equilibrium is assumed to be maintained throughout bulk and surface motion at all times. The governing equation for this condition in strong form is as follows:

$$\boldsymbol{\nabla}_{\mathbf{X}}\cdot\mathbf{P}+\mathbf{B}=0\quad\text{in}\quad V \tag{2.9}$$

$$\mathbf{P}\cdot\mathbf{N}-\widetilde{\boldsymbol{\nabla}}_{\widetilde{\mathbf{X}}}\cdot\widetilde{\mathbf{P}}=\mathbf{T}\quad\text{on}\quad S_{\mathrm{T}} \tag{2.10}$$

$$\mathbf{u}=\mathbf{u}_p\quad\text{on}\quad S_{\mathrm{u}} \tag{2.11}$$

$$[[\widetilde{\mathbf{P}}\cdot\widetilde{\mathbf{N}}]]=0\quad\text{on}\quad L \tag{2.12}$$

where $\mathbf{P}$ and $\widetilde{\mathbf{P}}$ are the first Piola–Kirchhoff stresses in bulk and on surface, $\mathbf{B}$ and $\mathbf{T}$ are the body force and the traction vector, and $\mathbf{u}_p$ is the prescribed displacement. S_{T} and S_{u} are the boundary surfaces where traction and displacement are prescribed, respectively. The local linear momentum balance between the film and substrate is illustrated in Fig. 2(b). Note that a Neumann-type boundary condition is also defined on boundary curves, where $[[\bullet]]$ indicates summation over surfaces intersecting on boundary curves (Kim et al., 2023b). The Neumann-type boundary condition is illustrated in Fig. 2(c).

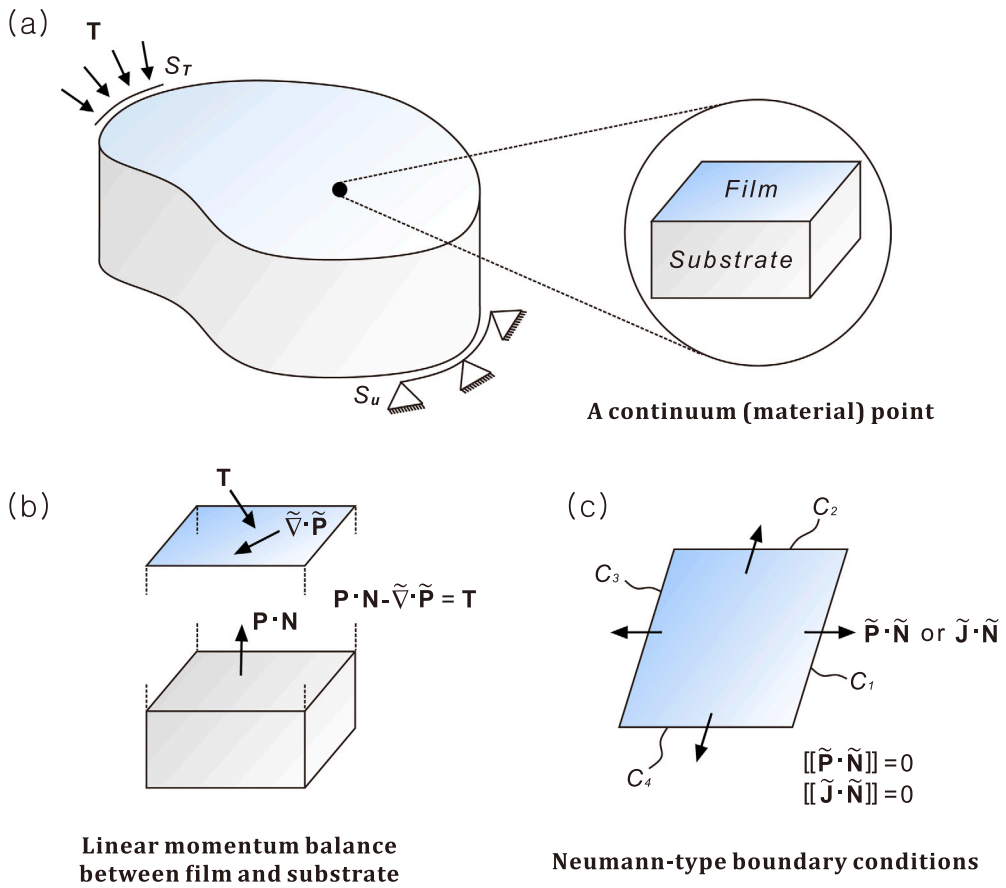

Fig. 2. Schematic representation of the local linear momentum balance and Neumann-type boundary conditions: (a) Illustration of a continuum point within the film–substrate system, (b) depiction of the local linear momentum balance between the film and substrate, and (c) visualization of the Neumann-type boundary conditions applied to the system.

2.3. Species balance

Here, we consider species balance only on the deforming surface of the system, as we consider that the bulk is impermeable; thus, we follow only surface diffusion kinetics. Through species (or mass) balance, the strong form for the corresponding governing equation is given by McBride et al. (2011), Kim et al. (2023b):

$$\dot{\tilde{C}} + \tilde{\nabla}_{\mathbf{X}} \cdot \tilde{\mathbf{J}} = \tilde{i} \quad \text{on} \quad S_{\tilde{C}} \tag{2.13}$$

$$\tilde{\mathbf{J}} = \tilde{\mathbf{J}}_p \quad \text{on} \quad L_{\tilde{J}} \tag{2.14}$$

$$[[\tilde{\mathbf{J}} \cdot \tilde{\mathbf{N}}]] = 0 \quad \text{on} \quad L \tag{2.15}$$

where $\tilde{C}$ represents the surface nominal concentration, which is the number of solvent moles per unit reference area. The overdot denotes the material time derivative. The term $\tilde{\mathbf{J}}$ stands for the surface nominal flux, denoting the number of solvent moles per unit time per unit reference length. The source/sink term is denoted as $\tilde{i}$. Eq. (2.13) describes the species balance on the surface, and for our model, we assume $\tilde{i} = 0$, signifying that the species are conserved. This implies that species neither enter the surface from the external environment nor exit from the interior bulk. Eq. (2.13) is, in turn, supplemented by the prescribed flux $\tilde{\mathbf{J}}_p$ (Eq. (2.14)), and the Neumann-type boundary condition (Eq. (2.15)), which is illustrated in Fig. 2(c). $S_{\tilde{C}}$ is the boundary surface where the species are balanced, and $L_{\tilde{J}}$ is the boundary curve where the surface flux is prescribed. Additionally, the initial condition is given by

$$\tilde{C}(\tilde{\mathbf{X}}, t = 0) = \tilde{C}_0 \tag{2.16}$$

where $\tilde{C}_0$ is the initial species concentration on the surface at time $t = 0$.

Remark 2 (*Neumann-type Boundary Condition for Surface Flux*)**.** It is important to note that $\tilde{i}$ may include contributions from external supply, production, or consumption, and can be written as

$$\tilde{i} = -[q - \mathbf{J} \cdot \mathbf{N}], \tag{2.17}$$

where q is an external source term and $\mathbf{J} \cdot \mathbf{N}$ represents the net species flux through the boundary. In this study, we consider a closed system with $q = 0$ and no source or sink term, i.e., $\tilde{i} = 0$. Therefore, the conservation condition requires the net surface flux across the boundary to vanish:

$$[[\tilde{\mathbf{J}} \cdot \tilde{\mathbf{N}}]] = 0, \tag{2.18}$$

where the double-bracket notation is used to represent the average and jump of a surface quantity (see Remark 1).

2.4. Thermodynamic considerations

We consider the free energy density for both bulk and surface, where we assume that the bulk free energy depends on deformation and viscous dissipation, while the surface free energy is function of deformation and species concentration (Holzapfel, 2002). On the other hand, since we are focusing on surface diffusion, the surface free energy can be decomposed into elastic and mixing parts (Hong et al., 2008), as follows

$$\Psi(\mathbf{F}, \mathbf{A}) \quad \text{and} \quad \tilde{\Psi}(\tilde{\mathbf{F}}, \tilde{C}) \tag{2.19}$$

where $\mathbf{A}$ is an internal variable (second-order tensor) to account for the dissipation process related to the viscoelastic deformation.

Considering a system that includes a viscoelastic substrate and a rigidly bonded porous film with species that can freely migrate within

the porous network, the rate of change of the system's free energy $\mathcal{G}$ has to account for several effects (Holzapfel, 2002; Gurtin et al., 2010; Hong et al., 2008; Kim et al., 2023b). This can be expressed as

$$\dot{\mathcal{G}} = \int_V \dot{\Psi}\,\mathrm{d}V + \int_S \dot{\widetilde{\Psi}}\,\mathrm{d}S - \int_V \mathbf{B}\cdot\dot{\mathbf{x}}\,\mathrm{d}V - \int_S \mathbf{T}\cdot\dot{\mathbf{x}}\,\mathrm{d}S - \int_S \widetilde{\mu}\,\widetilde{i}\,\mathrm{d}S \tag{2.20}$$

where the third and fourth terms are the rate of mechanical work by the body force $\mathbf{B}$ and traction vector $\mathbf{T}$, and the fifth term is the rate of chemical work by the surface chemical potential $\widetilde{\mu}$. The overdot denotes the material time derivative. Note that thermodynamics dictate that the free energy of the system should not increase ($\dot{\mathcal{G}} \le 0$), and we here consider two dissipation processes: viscous deformation of substrate and the solvent diffusion on film.

Substituting Eqs. (2.9), (2.10) and (2.13) into Eq. (2.20), the rate of change of the free energy of the system can be expressed as follows,

$$\dot{\mathcal{G}} = \int_V \dot{\Psi}\,\mathrm{d}V + \int_S \dot{\widetilde{\Psi}}\,\mathrm{d}S - \int_V \mathbf{P} : \dot{\mathbf{F}}\,\mathrm{d}V - \int_S \widetilde{\mathbf{P}} : \dot{\widetilde{\mathbf{F}}}\,\mathrm{d}S - \int_S \widetilde{\mu}\dot{\widetilde{C}}\,\mathrm{d}S + \int_S \widetilde{\mathbf{J}}\cdot\widetilde{\boldsymbol{\nabla}}_{\widetilde{\mathbf{X}}}\widetilde{\mu}\,\mathrm{d}S \le 0 \tag{2.21}$$

where $\{:\}$ denotes the double contraction. Using the chain-rule, the rate of bulk and surface free energy densities can be expressed as

$$\dot{\Psi} = \frac{\partial\Psi}{\partial\mathbf{F}} : \dot{\mathbf{F}} + \frac{\partial\Psi}{\partial\mathbf{A}} : \dot{\mathbf{A}} \quad \text{and} \quad \dot{\widetilde{\Psi}} = \frac{\partial\widetilde{\Psi}}{\partial\widetilde{\mathbf{F}}} : \dot{\widetilde{\mathbf{F}}} + \frac{\partial\widetilde{\Psi}}{\partial\widetilde{C}}\dot{\widetilde{C}} \tag{2.22}$$

Substituting Eq. (2.22) into Eq. (2.21), and rearranging terms yields

$$\dot{\mathcal{G}} = \int_V \left(\frac{\partial\Psi}{\partial\mathbf{F}} - \mathbf{P}\right) : \dot{\mathbf{F}}\,\mathrm{d}V + \int_S \left(\frac{\partial\widetilde{\Psi}}{\partial\widetilde{\mathbf{F}}} - \widetilde{\mathbf{P}}\right) : \dot{\widetilde{\mathbf{F}}}\,\mathrm{d}S + \int_S \left(\frac{\partial\widetilde{\Psi}}{\partial\widetilde{C}} - \widetilde{\mu}\right)\dot{\widetilde{C}}\,\mathrm{d}S + \int_S \widetilde{\mathbf{J}}\cdot\widetilde{\boldsymbol{\nabla}}_{\widetilde{\mathbf{X}}}\widetilde{\mu}\,\mathrm{d}S + \int_V \frac{\partial\Psi}{\partial\mathbf{A}} : \dot{\mathbf{A}}\,\mathrm{d}V \le 0 \tag{2.23}$$

where each integral represents a distinct mechanism of energy dissipation, associated with mechanical and chemical works. The inequality must hold at every point of the continuum body and at all times during a thermodynamic process. To satisfy the constraint, the Coleman-Noll procedure (Holzapfel, 2002) states that each integrand in Eq. (2.23) to be either negative or equal to zero.

From the first three terms in Eq. (2.23) we obtain the following constitutive relations

$$\mathbf{P} = \frac{\partial\Psi(\mathbf{F},\mathbf{A})}{\partial\mathbf{F}}, \quad \widetilde{\mathbf{P}} = \frac{\partial\widetilde{\Psi}(\widetilde{\mathbf{F}},\widetilde{C})}{\partial\widetilde{\mathbf{F}}} \quad \text{and} \quad \widetilde{\mu} = \frac{\partial\widetilde{\Psi}(\widetilde{\mathbf{F}},\widetilde{C})}{\partial\widetilde{C}} \tag{2.24}$$

for the bulk and surface first Piola–Kirchhoff stresses tensors, and the surface chemical potentials, respectively. Additionally, to maintain that the fourth term in Eq. (2.23) remains to be negative or zero, we adopt a kinetic law for diffusion on surface (Kim et al., 2023b). This allows us to maintain negative semi-definiteness and describes the consistent species diffusion that is driven by gradients of chemical potential.

$$\widetilde{\mathbf{J}} = -\widetilde{\mathbf{M}}\cdot\widetilde{\boldsymbol{\nabla}}_{\widetilde{\mathbf{X}}}\widetilde{\mu} \tag{2.25}$$

Here, $\widetilde{\mathbf{M}}$ stands for the surface mobility tensor, which we will later specialize to fully define the constitutive laws governing solvent diffusion on surface. Finally, the non-equilibrium thermodynamic process represented by the last term in Eq. (2.23) is characterized by the internal variable for viscoelastic response.

$$\frac{\partial\Psi}{\partial\mathbf{A}} : \dot{\mathbf{A}} \le 0 \tag{2.26}$$

In the subsequent section, we will specify the evolution of the internal variable $\mathbf{A}$ to define the constitutive relations for viscoelastic deformation of substrate.

3. Specific material model

In this study, we make specific selections for the surface and bulk free energy densities, along with their corresponding constitutive laws and the definition of mobility tensors. Our focus is on a compressible viscoelastic substrate, and a hydrogel film that is rigidly bonded and allows surface diffusion kinetics coupled with its deformation.

3.1. Bulk free energy density for soft substrate

We consider the decomposition of the bulk free energy into elastic and viscoelastic components, denoted as $\Psi(\mathbf{F},\mathbf{A}) = \Psi_e(\mathbf{F}) + \Psi_v(\overline{\mathbf{F}},\mathbf{A})$. For the elastic part, we employ the compressible hyperelastic model for the bulk free energy density (Holzapfel, 2002; Kim et al., 2023b). Regarding the viscoelastic part, we adopt a finite viscoelastic model (Linder et al., 2011). This choice allows us to account for the viscoelastic behavior of the material within our formulation.

$$\Psi_e(\mathbf{F}) = \frac{G}{2}(I_1 - 3 - 2\ln J) + \frac{K}{2}(J-1)^2 \tag{3.1}$$

$$\Psi_v(\mathbf{F},\mathbf{A}) = \frac{G_v}{2}\left(\mathbf{A} : \overline{\mathbf{C}} - 3 - \ln(\det\mathbf{A})\right) \tag{3.2}$$

where G and K are the shear and bulk moduli, and G_v is the viscous modulus for the substrate. It is worth emphasizing that the viscoelastic free energy density Ψ_v depends on two key variables: (i) The modified right Cauchy–Green tensor $\overline{\mathbf{C}} = \overline{\mathbf{F}}^{\mathrm{T}}\overline{\mathbf{F}}$, which indicates that the material's volumetric response remains fully elastic. (ii) The internal variable $\mathbf{A}$, which describes the material's relaxation behavior and encompasses viscoelastic effects.

3.2. Surface free energy density for hydrogel film

Building upon the previous approach (McBride et al., 2011; Lucantonio et al., 2013, 2016; Kim et al., 2023b,a), we decompose the surface free energy density of the polymer film into two distinct components: $\widetilde{\Psi}(\widetilde{\mathbf{F}},\widetilde{C}) = \widetilde{\Psi}_e(\widetilde{\mathbf{F}}) + \widetilde{\Psi}_m(\widetilde{C})$. Unlike the standard Flory free energy (Flory and Rehner Jr., 1943; Flory, 1961), which is defined with respect to a dry, stress-free reference configuration, our study considers the "initial state" of the hydrogel as fully swollen and attached to the substrate. This initial state is not stress-free due to swelling-induced deformation. To account for this, we introduce the "initial swelling stretch" $\widetilde{\lambda}_0$, which quantifies the volumetric change due to swelling. The relationship between the "reference state" (dry) and "initial state" (swollen) is shown in (Fig. 1).

$$\widetilde{\Psi}_e(\widetilde{\mathbf{F}}) = \frac{1}{\widetilde{J}_0}\frac{\widetilde{G}}{2}\left[\widetilde{\lambda}_0^2\,\widetilde{I}_1 - 2 - 2\ln\left(\widetilde{J}_0\widetilde{J}\right)\right] \tag{3.3}$$

$$\widetilde{\Psi}_m(\widetilde{C}) = -\frac{\widetilde{\beta}}{\widetilde{J}_0}\frac{k_B T}{\widetilde{\Omega}}\left[\widetilde{\Omega}\widetilde{J}_0\widetilde{C}\,\ln\left(\frac{1+\widetilde{\Omega}\widetilde{J}_0\widetilde{C}}{\widetilde{\Omega}\widetilde{J}_0\widetilde{C}}\right) + \frac{\widetilde{\chi}}{1+\widetilde{\Omega}\widetilde{J}_0\widetilde{C}}\right] \tag{3.4}$$

where $\widetilde{\Psi}_e$ and $\widetilde{\Psi}_m$ are the free energy densities per unit area at initial (swollen) state, and $\widetilde{\lambda}_0$ and $\widetilde{J}_0$ are initial stretch and Jacobian determinant of the surface deformation gradient with respect to the dry configuration of the film. $\widetilde{G} = \widetilde{N}k_B T$ denotes the surface shear modulus at dry state, where $\widetilde{N}$ is the number of polymer chains on the film hydrogel per unit area, k_B is the Boltzmann's constant, and T is an absolute temperature. $\widetilde{\Omega}$ corresponds to the area occupied by a solvent molecule on the surface, and $\widetilde{\chi}$ is a surface Flory parameter quantifying the degree of polymer-solvent mixing. The parameter $\widetilde{\beta}$ is introduced to account for the number of 2D layers in the surface zone (Kim et al., 2023b).

The absorption of solvent into the hydrogel film induces volumetric changes. In modeling the kinematics of a swelling material surface, both thickness variation and areal change should be considered (Lucantonio et al., 2016). However, in this study, we neglect thickness variation due to the thinness of the film. As a result, the species concentration is assumed to be solely proportional to the areal change. Following Hong et al. (2008), Kim et al. (2023b), we assume that the polymer chains and the diffusion species are individually incompressible. The hydrogel, being a condensed matter with negligible void space, experiences area changes primarily due to species diffusion:

$$1 + \widetilde{\Omega}\widetilde{C}_0 = \widetilde{J}_0 \quad \text{and} \quad 1 + \widetilde{\Omega}\left(\widetilde{C} - \widetilde{C}_0\right) = \widetilde{J} \Rightarrow \widetilde{C} = \widetilde{C}_0 + \frac{\widetilde{J}-1}{\widetilde{\Omega}} \tag{3.5}$$

where the initial concentration $\widetilde{C}_0$ is determined by the initial stretch $\widetilde{\lambda}_0$ that can be determined by the initial chemical potential $\widetilde{\mu}_0$, and their analytical expression can be found in Appendix A.

Remarks: Energetic consideration in a film/substrate system

For the substrate, we assume that the initial state coincides with the reference (stress-free) state. However, for the porous film, the reference (dry) state and the initial (swollen) state are different. It is important to note that the free-swollen film is attached in a planar fashion to the substrate, and the general kinematic description takes that state as the initial state. To account for the different reference states and to simultaneously describe the mechanical behavior of the film and substrate, it is necessary to incorporate the initial swelling into the free energy formulation of the film. This consideration leads to the inclusion of the factor $1/\widetilde{J}_0$ in Eqs. (3.3) and (3.4) (a detailed discussion can be found in Appendix A). It is also important to note that the kinematics of proposed model does not explicitly consider the film's thickness, i.e., the surface energy is derived in 2D while attached to the 3D substrate. However, the thickness effect of the film is accounted for by introducing the parameter $\widetilde{\beta}$ in Eq. (3.4). Additionally, the species diffusion in thin hydrogel films is assumed to occur within the film layer, neglecting diffusion in the thickness direction.

3.3. Evolution equation for viscoelasticity

To fully define the constitutive relation for the viscoelastic response as described in Eq. (2.26), governing the free energy relaxation in Eq. (3.2), we specify the evolution of internal variable $\mathbf{A}$ as follows (Linder et al., 2011)

$$\dot{\mathbf{A}} = \frac{1}{\tau_r}\left(\overline{\mathbf{C}}^{-1} - \mathbf{A}\right), \quad \mathbf{A}\left(\mathbf{X}, t_0\right) = \mathbf{I} \tag{3.6}$$

where τ_r is the characteristic time scale of relaxation. When $\overline{\mathbf{C}}^{-1} = \mathbf{A}$ is satisfied, it indicates that the system reaches equilibrium and the viscoelastic response is fully relaxed.

3.4. Constitutive equations

Since the chemical boundary conditions for hydrogels are often specified in terms of chemical potential or diffusion flux (proportional to the gradient of chemical potential), it is convenient to use the chemical potential (instead of solvent concentration) as an independent variable in the finite element formulation. Additionally, this allows us to avoid C^1 continuity requirements (see Appendix B). For this purpose, we rewrite the free energy densities as a function of the deformation gradient and chemical potential through a Legendre transform (Hong et al., 2008, 2009; Kim et al., 2023b), which replaces a variable with its thermodynamic conjugate:

$$\widetilde{\Psi}(\widetilde{\mathbf{F}}, \widetilde{\mu}) = \widetilde{\Psi}(\widetilde{\mathbf{F}}, \widetilde{C}) - \widetilde{\mu}\widetilde{C} \tag{3.7}$$

After the Legendre transform, similar to Eq. (2.24), the constitutive relations can be rewritten as follows:

$$\mathbf{P} = \frac{\partial \Psi(\mathbf{F}, \mathbf{A})}{\partial \mathbf{F}}, \quad \widetilde{\mathbf{P}} = \frac{\partial \widetilde{\Psi}(\widetilde{\mathbf{F}}, \widetilde{\mu})}{\partial \widetilde{\mathbf{F}}} \quad \text{and} \quad \widetilde{C} = -\frac{\partial \widetilde{\Psi}(\widetilde{\mathbf{F}}, \widetilde{\mu})}{\partial \widetilde{\mu}} \tag{3.8}$$

It is important to note that $\widetilde{\mathbf{P}}$ must be modified to reflect the incompressibility constraint (Eq. (3.5)) used to eliminate $\widetilde{C}$ as an independent variable, since the nonlinear algebraic equation in Eq. (3.11) does not yield a closed-form solution. The derivation of the surface first Piola–Kirchhoff stress can be found in Appendix A. The specific constitutive relations are obtained as follows:

$$\mathbf{P} = G\left(\mathbf{F} - \mathbf{F}^{-\mathrm{T}}\right) + K\left(J-1\right)J\mathbf{F}^{-\mathrm{T}} + G_v J^{-2/3}\,\mathbf{F}\cdot\left[\mathbf{A} - \frac{1}{3}\left(\mathbf{A} : \mathbf{C}\right)\mathbf{C}^{-1}\right] \tag{3.9}$$

$$\begin{aligned}
&\widetilde{\mathbf{P}} = \frac{\widetilde{G}}{\widetilde{J}_0}\left(\widetilde{\lambda}_0^2\widetilde{\mathbf{F}} + \widetilde{\alpha}\widetilde{J}\widetilde{\mathbf{F}}^{-\mathrm{T}}\right),\\
&\widetilde{\alpha} = -\frac{1}{\widetilde{J}} + \frac{\widetilde{\beta}}{\widetilde{N}\widetilde{\Omega}}\left[\widetilde{J}_0 \ln\left(1 - \frac{1}{\widetilde{J}_0\widetilde{J}}\right) + \frac{1}{\widetilde{J}} + \frac{\widetilde{\chi}}{\widetilde{J}_0\widetilde{J}^2} - \frac{\widetilde{J}_0}{\widetilde{\beta}}\frac{\widetilde{\mu}}{k_B T}\right]
\end{aligned} \tag{3.10}$$

$$\widetilde{\mu} = \widetilde{\beta}k_B T\left[\ln\left(\frac{\widetilde{\Omega}\widetilde{J}_0\widetilde{C}}{1+\widetilde{\Omega}\widetilde{J}_0\widetilde{C}}\right) + \frac{1}{1+\widetilde{\Omega}\widetilde{J}_0\widetilde{C}} + \frac{\widetilde{\chi}}{\left(1+\widetilde{\Omega}\widetilde{J}_0\widetilde{C}\right)^2}\right] \Rightarrow \widetilde{C} = \widetilde{C}(\widetilde{\mu}) \tag{3.11}$$

where these are the specific forms of the constitutive relations for the first Piola–Kirchhoff stresses and the chemical potential on the surface. Although Eq. (3.11) is derived based on thermodynamic considerations, it is not employed in the numerical implementation due to its nonlinear structure and lack of a closed-form solution. Instead, the incompressibility condition in Eq. (3.5) is used to determine the surface concentration $\widetilde{C}$ as a function of deformation. This is justified by the assumption of negligible voids in the hydrogel and the incompressibility of both the polymer and solvent components.

3.5. Surface diffusion

To complete the constitutive relation for the kinetic law governing surface diffusion in Eq. (2.25), we specify the surface mobility tensor as follows:

$$\widetilde{\mathbf{M}} = \frac{\widetilde{C}\widetilde{D}}{k_B T}\widetilde{\mathbf{C}}^{-1} \tag{3.12}$$

The diffusion coefficient of the solvent molecules $\widetilde{D}$ on the surface is assumed to be isotropic and independent of the deformation and concentration as the simplest approximation (Kim et al., 2023b).

4. Mixed finite element formulation

This section outlines the finite element formulation based on the nonlinear theory presented in Sections 2 and 3 using FEniCS (Logg et al., 2012; Alnæs et al., 2015) for the implementation. The weak form of the governing equations is introduced, followed by an explanation of the normalization, discretization, and the nonlinear solution process. It is important to note that, in this section, we concentrate on the surface diffusion coupled with the deformation of the substrate; therefore, we do not consider the source terms, i.e., $\widetilde{i} = 0$.

4.1. Two-field weak form

The weak form of the problem is obtained by using a set of test functions, which satisfy the necessary integrability conditions (Hughes, 2012). By multiplying Eqs. (2.9) and (2.13) with the test functions $\delta\mathbf{u}$ and $\delta\widetilde{\mu}$, and integrating over the domain, respectively, then we obtain that

$$\int_V \mathbf{P} : \boldsymbol{\nabla}_{\mathbf{X}}\delta\mathbf{u}\,\mathrm{d}V + \int_S \widetilde{\mathbf{P}} : \widetilde{\boldsymbol{\nabla}}_{\widetilde{\mathbf{X}}}\delta\mathbf{u}\,\mathrm{d}S = 0 \tag{4.1}$$

$$\int_S \dot{\widetilde{C}}\,\delta\mu\,\mathrm{d}S - \int_S \widetilde{\mathbf{J}}\cdot\widetilde{\boldsymbol{\nabla}}_{\widetilde{\mathbf{X}}}\delta\mu\,\mathrm{d}S = 0 \tag{4.2}$$

The statement of the weak form is to find the trial functions, $\{\mathbf{u}, \widetilde{\mu}\} \in \mathcal{S}_u \times \mathcal{S}_{\widetilde{\mu}}$, such that the integrals in Eqs. (4.1) and (4.2) are satisfied for any permissible test functions, $\{\delta\mathbf{u}, \delta\widetilde{\mu}\} \in \mathcal{V}_{\delta u} \times \mathcal{V}_{\delta\widetilde{\mu}}$. We note that the mobility tensor $\widetilde{\mathbf{M}}$ is inversely proportional to the Green deformation tensor $\widetilde{\mathbf{C}}^{-1}$ (Eq. (3.12)), which accounts for finite deformation and its effect on the porosity of the film. This dependence introduces a constitutive coupling between deformation and diffusion. Additionally, the incompressibility condition $\widetilde{J} = 1 + \widetilde{\Omega}(\widetilde{C} - \widetilde{C}_0)$ (Eq. (3.5)) introduces a geometric coupling between deformation and the surface concentration $\widetilde{C}$. Consequently, the weak forms of deformation (Eq. (4.1)) and surface diffusion (Eq. (4.2)) are fully coupled, which is addressed by solving them simultaneously using the monolithic solver in Eq. (4.20). We denote the set of all functions that are admissible trial functions by $\mathcal{S}_u$ and $\mathcal{S}_{\widetilde{\mu}}$,

$$\mathcal{S}_u = \{\mathbf{u} \,|\, \mathbf{u} \in \mathcal{H}^1,\ \mathbf{u} = \mathbf{u}_p \text{ on } S_u\} \tag{4.3}$$

$$S_{\widetilde{\mu}} = \{\widetilde{\mu} \,|\, \widetilde{\mu} \in \mathcal{H}^1,\ \widetilde{\mu} = \widetilde{\mu}_p \text{ on } S_{\widetilde{\mu}}\} \tag{4.4}$$

where $\mathbf{u}_p$ and $\widetilde{\mu}_p$ are the prescribed values on Dirichlet boundary conditions. Similarly, the set of all admissible test functions are denoted by $\mathcal{V}_{\delta u}$ and $\mathcal{V}_{\delta\widetilde{\mu}}$,

$$\mathcal{V}_{\delta u} = \{\delta\mathbf{u} \,|\, \delta\mathbf{u} \in \mathcal{H}^1,\ \delta\mathbf{u} = 0 \text{ on } S_u\} \tag{4.5}$$

$$\mathcal{V}_{\delta\widetilde{\mu}} = \{\delta\widetilde{\mu} \,|\, \delta\widetilde{\mu} \in \mathcal{H}^1,\ \delta\widetilde{\mu} = 0 \text{ on } S_{\widetilde{\mu}}\} \tag{4.6}$$

where $\mathcal{H}^1$ denotes Sobolev spaces of degree one.

4.2. Normalization

For the finite element simulations in the following section, all variables and parameters are normalized, as denoted by the overhat notation $\{\widehat{\bullet}\}$. All lengths are normalized by a characteristic dimension, $H = \widetilde{G}/G$ (shear moduli ratio). The chemical potential and stresses are normalized as follows,

$$\widehat{\mathbf{P}} = \frac{\mathbf{P}}{G}, \quad \widehat{\widetilde{\mathbf{P}}} = \frac{\widetilde{\mathbf{P}}}{\widetilde{G}}, \quad \widehat{\widetilde{\mu}} = \frac{\widetilde{\mu}}{\widetilde{\beta} k_B T} \tag{4.7}$$

Solvent concentration and time are normalized as follows,

$$\widehat{\widetilde{C}} = \widetilde{\Omega}\widetilde{C}, \quad \hat{t} = \frac{t}{\tau_d} \tag{4.8}$$

where $\tau_d = \widetilde{H}^2/\widetilde{D}$ is the characteristic time scale of diffusion.

By substituting the normalized variables into the weak forms in Eqs. (4.1) and (4.2), we can obtain the normalized weak forms.

$$\int_V \widehat{\mathbf{P}} : \boldsymbol{\nabla}_{\widehat{\mathbf{X}}} \delta\widehat{\mathbf{u}} \, \mathrm{d}\widehat{V} + \int_S \widehat{\widetilde{\mathbf{P}}} : \widetilde{\boldsymbol{\nabla}}_{\widehat{\mathbf{X}}} \delta\widehat{\mathbf{u}} \, \mathrm{d}\widehat{S} = 0 \tag{4.9}$$

$$\int_S \frac{d\widehat{\widetilde{C}}}{d\hat{t}} \delta\widehat{\widetilde{\mu}} \, \mathrm{d}\widehat{S} - \int_S \widehat{\widetilde{\mathbf{J}}} \cdot \frac{\partial \delta\widehat{\widetilde{\mu}}}{\partial \widehat{\widetilde{\mathbf{X}}}} \, \mathrm{d}\widehat{S} = 0 \tag{4.10}$$

where the normalized flux is defined by

$$\widehat{\widetilde{\mathbf{J}}} = -\widehat{\widetilde{C}}\widetilde{\mathbf{C}}^{-1} \cdot \widetilde{\boldsymbol{\nabla}}_{\widehat{\mathbf{X}}} \widehat{\widetilde{\mu}} \tag{4.11}$$

4.3. Temporal discretization

To update the species balance, the backward Euler scheme is used to integrate Eq. (4.10) over time:

$$\int_S \left[\frac{1}{\Delta\hat{t}} \left(\widehat{\widetilde{C}}^{\hat{t}+\Delta\hat{t}} - \widehat{\widetilde{C}}^{\hat{t}} \right) \delta\widehat{\widetilde{\mu}} - \int_S \widehat{\widetilde{\mathbf{J}}}^{\hat{t}+\Delta\hat{t}} \cdot \widetilde{\boldsymbol{\nabla}}_{\widehat{\mathbf{X}}} \delta\widehat{\widetilde{\mu}} \right] \mathrm{d}\widehat{S} = 0 \tag{4.12}$$

where the superscripts indicate the time step, at the current time step $(\hat{t} + \Delta\hat{t})$ or the previous step $\hat{t}$. We can combine Eqs. (4.9) and (4.12) as follows:

$$\begin{aligned} &\int_V \widehat{\mathbf{P}} : \boldsymbol{\nabla}_{\widehat{\mathbf{X}}} \delta\widehat{\mathbf{u}} \, \mathrm{d}\widehat{V} + \int_S \widehat{\widetilde{\mathbf{P}}} : \widetilde{\boldsymbol{\nabla}}_{\widehat{\mathbf{X}}} \delta\widehat{\mathbf{u}} \, \mathrm{d}\widehat{S} \\ &+ \int_S \left(\widehat{\widetilde{C}} - \widehat{\widetilde{C}}^{\hat{t}} \right) \delta\widehat{\widetilde{\mu}} \, \mathrm{d}\widehat{S} + \Delta\hat{t} \int_S \left(\widehat{\widetilde{C}}\widetilde{\mathbf{C}}^{-1} \cdot \widehat{\widetilde{\boldsymbol{\nabla}}}_{\widehat{\mathbf{X}}} \widehat{\widetilde{\mu}} \right) \cdot \widehat{\widetilde{\boldsymbol{\nabla}}}_{\widehat{\mathbf{X}}} \delta\widehat{\widetilde{\mu}} \, \mathrm{d}\widehat{S} = 0 \end{aligned} \tag{4.13}$$

where the superscript $(\hat{t} + \Delta\hat{t})$ is omitted for all the terms at the current time step and $\widehat{C}^{\hat{t}}$ and $\widehat{\widetilde{C}}^{\hat{t}}$ are the species concentration at the previous time step in the bulk and on the surface.

Note that, we also adopt the backward Euler scheme with Eq. (3.6) to update the viscoelastic response, resulting in the update of the internal variable $\mathbf{A}$.

$$\mathbf{A} = \frac{1}{1 + (\tau_d/\tau_r)\,\Delta\hat{t}} \left[\mathbf{A}^{\hat{t}} + (\tau_d/\tau_r)\,\Delta\hat{t}\, \overline{\mathbf{C}}^{-1} \right] \tag{4.14}$$

where the terms without the superscript are at the current time step, and $\mathbf{A}^{\hat{t}}$ is the internal variable at the previous time step.

4.4. Spatial discretization

A mixed finite element method is employed to concurrently solve for the normalized displacement and surface chemical potential fields. To circumvent potential numerical instabilities associated with the mixed method, appropriate spatial discretization techniques are essential (Kim et al., 2023b,a). In this context, we adopt the Taylor-Hood element (Taylor and Hood, 1973), where the displacement and surface chemical potential are interpolated using quadratic and linear orders, respectively. It is important to note that linear interpolation is only utilized on the surface, where hydrogel film is applied.

The normalized displacement and chemical potential are interpolated through the domain of interest as

$$\widehat{\mathbf{u}} = \mathbf{H}^{\hat{\mathbf{u}}} \widehat{\mathbf{u}}^n, \quad \widehat{\widetilde{\mu}} = \mathbf{H}^{\hat{\widetilde{\mu}}} \widehat{\widetilde{\boldsymbol{\mu}}}^n \tag{4.15}$$

where $\mathbf{H}^{\hat{\mathbf{u}}}$ and $\mathbf{H}^{\hat{\widetilde{\mu}}}$ are the shape functions, $\widehat{\mathbf{u}}^n$ and $\widehat{\widetilde{\boldsymbol{\mu}}}^n$ are the nodal values of the normalized displacement, chemical potential, respectively. The test functions are discretized in the same way

$$\delta\widehat{\mathbf{u}} = \mathbf{H}^{\hat{\mathbf{u}}} \delta\widehat{\mathbf{u}}^n, \quad \delta\widehat{\mu} = \mathbf{H}^{\hat{\widetilde{\mu}}} \delta\widehat{\widetilde{\boldsymbol{\mu}}}^n \tag{4.16}$$

The stresses, concentrations, and fluxes are evaluated at integration points, depending on the gradients of the displacement and chemical potential via the constitutive relations. Taking the gradient of Eq. (4.15), we obtain that

$$\boldsymbol{\nabla}_{\widehat{\mathbf{X}}} \widehat{\mathbf{u}} = \boldsymbol{\nabla}_{\widehat{\mathbf{X}}} \mathbf{H}^{\hat{\mathbf{u}}} \widehat{\mathbf{u}}^n = \mathbf{B}^{\hat{\mathbf{u}}} \widehat{\mathbf{u}}^n \tag{4.17}$$

$$\boldsymbol{\nabla}_{\widehat{\mathbf{X}}} \widehat{\widetilde{\mu}} = \boldsymbol{\nabla}_{\widehat{\mathbf{X}}} \mathbf{H}^{\hat{\widetilde{\mu}}} \delta\widehat{\widetilde{\boldsymbol{\mu}}}^n = \mathbf{B}^{\hat{\widetilde{\mu}}} \widehat{\widetilde{\boldsymbol{\mu}}}^n \tag{4.18}$$

where $\mathbf{B}^{\hat{\mathbf{u}}}$ and $\mathbf{B}^{\hat{\widetilde{\mu}}}$ are the gradients of the shape functions.

4.5. Nonlinear solution

The weak form in Eq. (4.13) can be expressed as a system of nonlinear equations,

$$\mathcal{N}(\mathbf{d}) = \mathbf{f} \quad \text{with} \quad \mathbf{d} = \left[\widehat{\mathbf{u}}^n \ \widehat{\widetilde{\boldsymbol{\mu}}}^n \right]^{\mathrm{T}} \tag{4.19}$$

Note that $\mathcal{N}(\mathbf{d})$ denotes the part of the weak form that is not known at current time step, and we take all the known quantities to the right-hand side and denote as $\mathbf{f}$ (which is known from previous time step). The residual of nonlinear equations in iteration step i is given by $\mathbf{R}_i = \mathbf{f} - \mathcal{N}(\mathbf{d}_i)$, which can be solved using the Newton–Raphson method. In particular, the procedure requires the calculation of the tangent Jacobian matrix at each iteration, namely,

$$\left. \frac{\partial \mathcal{N}}{\partial \mathbf{d}} \right|_{\mathbf{d}_i} = \begin{bmatrix} \mathbf{K}^{\hat{\mathbf{u}}\hat{\mathbf{u}}} & \mathbf{K}^{\hat{\mathbf{u}}\hat{\widetilde{\mu}}} \\ \mathbf{K}^{\hat{\widetilde{\mu}}\hat{\mathbf{u}}} & \mathbf{K}^{\hat{\widetilde{\mu}}\hat{\widetilde{\mu}}} \end{bmatrix} \tag{4.20}$$

The coupled system in Eq. (4.20) can be solved either through a fully coupled "monolithic" method or a sequentially solved "staggered" method. The monolithic scheme is unconditionally stable with the backward Euler time-stepping. For these reasons, although the staggered solution scheme has the advantage of lower computational cost and utilization of existing solvers, we choose the monolithic method in this study.

In this study, the governing equations are implemented using FEniCS, an open-source platform for solving partial differential equations (PDEs) via the finite element method (FEM). Unlike commercial software, FEniCS offers flexibility to define new PDEs and constitutive laws, enabling the implementation of novel formulations. For example, the surface kinematics and diffusion in the present study are not available in the commercial software. FEniCS version 2019.2.0 (Logg et al., 2012; Alnæs et al., 2015) is used to numerically solve the coupled non-linear equations via the Portable Extensible Toolkit for Scientific Computations (PETSc) Scalable Nonlinear Equations Solvers (SNES) interface (Balay et al., 2019). This process repeats until a level of convergence specified within the SNES solver. At each iteration,

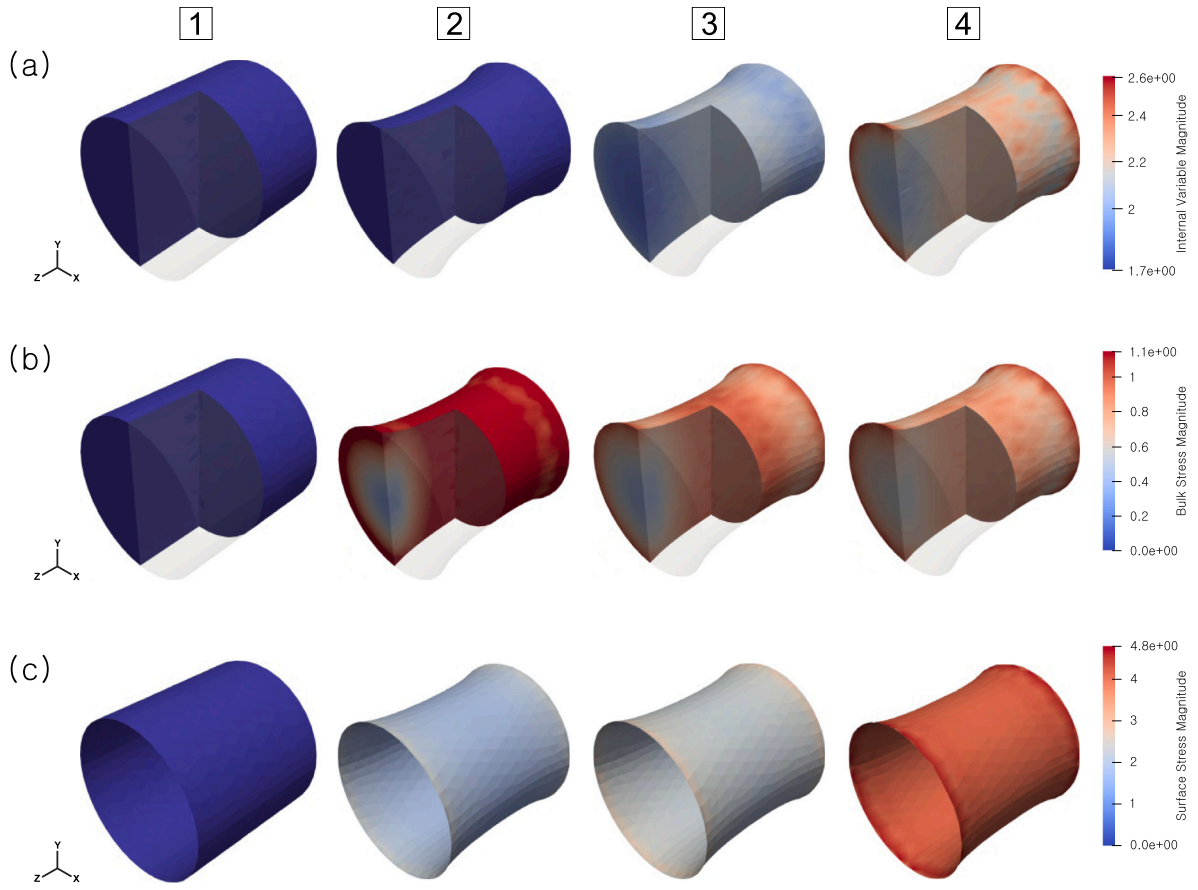

Fig. 3. Temporal sequence of (a) internal variable, (b) bulk stress, and (c) surface stress during the tension of a bar, with all variables normalized. The images are captured at normalized times $t/\tau = 0.0$, 0.01, 2.0, and 1.9×10^6 from left to right, labeled as Step 1, 2, 3, and 4, respectively.

the block Jacobian matrices are set up using Multiphenics (Ballarin, 2019), a python library that also facilitates the definition of boundary restricted variables within FEniCS, a feature necessary for dealing in our case with the surface concentration.

5. Numerical examples

We explore the transient responses of three initial and boundary value problems, involving the viscoelasticity of a soft substrate and the surface diffusion of a hydrogel thin film (Fig. 1 for general setup). The numerical studies include: (1) uniaxial tension of a cylindrical bar, (2) bending of a rectangular beam, and (3) rigid sphere indentation of a planar film/substrate system. In these examples, we consider $k_B T = 4 \times 10^{-21}\,\mathrm{J/mol}$. For the soft substrate, the shear and bulk moduli are set as $G = 1.0\,\mathrm{N/m^2}$ and $K = 2.16\,\mathrm{N/m^2}$, leading to a Poisson's ratio of $\nu = 0.3$. Additionally, the viscous modulus is considered as $G_v = 1.0\,\mathrm{N/m^2}$. Regarding the hydrogel film, the surface shear modulus at dry state is assumed to be $\widetilde{G} = 10^{-2}\,\mathrm{N/m}$, and characteristic dimensions of $H = 10^{-2}\,\mathrm{m}$ and $\widetilde{N}\widetilde{\Omega}/\widetilde{\beta} = 10^{-3}$ (dimensionless). This study focuses on the surface diffusion pattern driven by substrate deformation. To minimize the impact of distinct time scales between surface diffusion and the viscoelastic effects of the substrate, the characteristic time scale is set as $\tau := \tau_d = \tau_r = 1.0\,\mathrm{sec}$.

To investigate the transient response that follows mechanical loading, we employ a two-stage process. In the first stage, we linearly ramp the displacement boundary condition from zero to its prescribed value within the time interval $t/\tau \in [0.0, 0.01]$. This interval is deliberately set small, representing only 1% of the characteristic time scale for surface diffusion and viscoelasticity responses. Therefore, in the first stage, the non-equilibrium processes are negligible. In the second stage, we exponentially increase the time steps $\Delta t/\tau$ until equilibrium is attained, while keeping the boundary conditions constant. This longer time step allows us to capture the surface diffusion and substrate relaxation processes as time progresses. The initial state of the hydrogel film is determined by setting the surface Flory parameter $\widetilde{\chi} = 0.7705$ and initial chemical potential $\widehat{\mu}_0 = 0$ (a fully swollen state). By solving the non-linear algebraic equation (Eq. (A.5) in Appendix A), the initial stretch is obtained as $\widetilde{\lambda}_0 \approx 1.41$; subsequently, the normalized initial solvent concentration is obtained by $\widehat{\widetilde{C}}_0 \approx 1.0$.

5.1. Uniaxial tension of a cylindrical bar

This example investigates the non-equilibrium response of a soft bar subject to uniaxial tension. At the undeformed state, the radius of circular cross-section is H and the length of the bar is $2H$. The soft bar is considered to be covered by a hydrogel film on its free surface but not on the clamped ends. Initially, the bar and film are stress-free, and the body force is ignored. The two-stage solution procedure detailed above is followed here. On end of the bar is clamped and held fixed, while the other end is clamped and displaced along the axis of the bar (Z axis). Prescribed displacement is linearly ramped for the first stage of the solution procedure, and held fixed for the remainder. The non-homogeneous deformation profile that the bar attains during loading, is what drives surface diffusion.

In Fig. 3, we present the temporal evolution of the finite element simulation for the internal variables, bulk and surface stresses. Simultaneously, in Fig. 4, we display the temporal evolution of surface chemical potential, concentration, and flux, with all values normalized. To focus on the contour plot on two sections of the interior along with the field on the surface, we have removed a quarter of the domain from

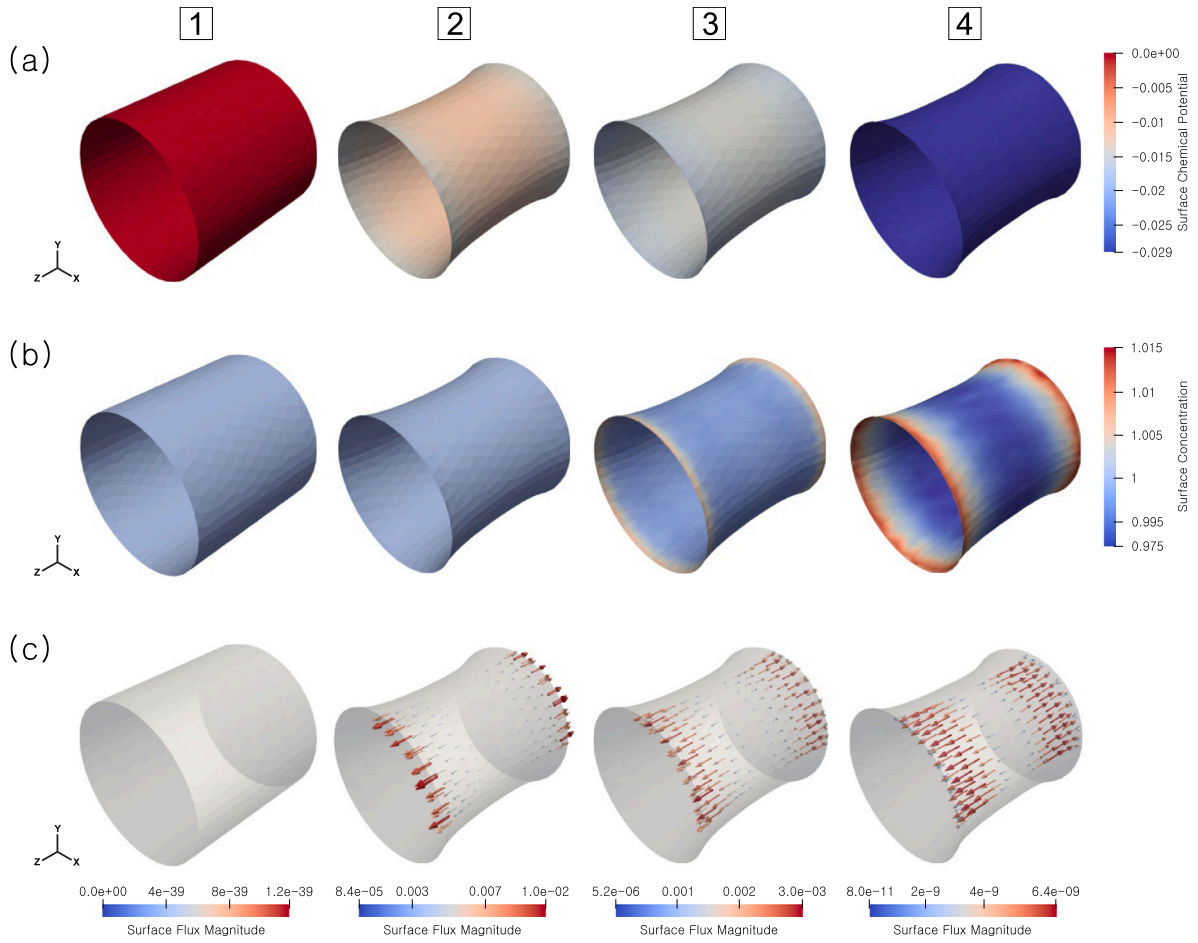

Fig. 4. Temporal sequence of (a) surface chemical potential, (b) surface concentration, and (c) surface flux during the tension of a bar, with all variables normalized. The images are captured at normalized times $t/\tau = 0.0$, 0.01, 2.0, and 1.9×10^6 from left to right, labeled as Step 1, 2, 3, and 4, respectively.

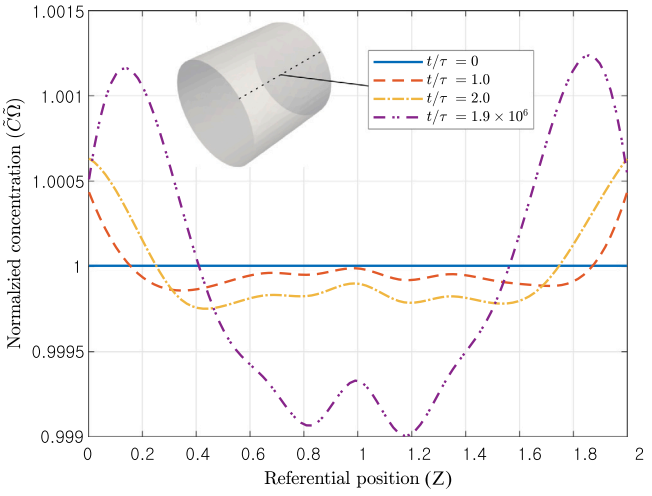

Fig. 5. Surface concentration profile during uniaxial tension of a cylindrical bar. Normalized surface concentrations ($\widetilde{\Omega}\widetilde{C}$) are tracked over normalized time (t/τ). Four representative profiles are shown at $t/\tau = 0.0$, 1.0, 2.0, and 1.9×10^6. The surface concentrations are measured at reference positions along the longitudinal direction (Z axis) of the bar.

the images of internal variables and bulk stresses in Figs. 3(a) and (b). For better visualization of surface fluxes in Fig. 4, we show the fluxes on a quarter of the bar. The images are captured at normalized times $t/\tau = 0.0$, 0.01, 2.0, and 1.9×10^6 from left to right, labeled as Step 1, 2, 3, and 4, respectively.

In Step 1 of Figs. 3 and 4, the bar represents the initial state, where the initial chemical potential is $\widehat{\widetilde{\mu}} = 0$, and the concentration is $\widehat{\widetilde{C}} = 1$. Step 2 of Figs. 3 and 4 corresponds to the time step where the boundary conditions are linearly ramped up to an end-to-end 10% extension. Note that Step 2 at time $t/\tau = 0.1$ is significantly smaller (7 orders of magnitude) compared to the equilibration time at Step 4, 1.9×10^6. As the bar is stretched, both bulk and surface stresses increase (Step 2 in Fig. 3(b) and (c)), and the surface chemical potential decreases (Step 2 in Fig. 4(a)). Although the time steps are very small in Step 2, the surface flux is observed at the boundary edges as a result of the deformation (Step 2 in Fig. 4(c)); however, the time step is so small that the surface concentration is nearly unchanged (Step 2 in Fig. 4(b)).

Beyond Step 2, and for the remainder of the transient response, the displacement boundary condition is held fixed at a 10% overall extension, and we exponentially increase the magnitude of the time steps toward equilibrium. In Step 3, the bar continues to deform primarily due to the viscoelastic relaxation of the substrate, but also due to the surface diffusion of the film. Specifically, the internal variable $\mathbf{A}$ increases (Fig. 3(a), Step 3), leading to the relaxation of bulk stress (Fig. 3(b), Step 3). This relaxation drives the surface diffusion of the film (Fig. 4(c), Step 3) and results in heterogeneous surface concentration (Fig. 4(b), Step 3). Interestingly, the surface stress increases (contrary to the stress drop in the bulk) because the film is assumed to not be viscoelastic (Fig. 3(c), Step 3). The system reaches its equilibrium state at Step 4. This is confirmed by the homogeneous chemical potential (Fig. 4(a), Step 4) and negligible surface flux (Fig. 4(c), Step 4).

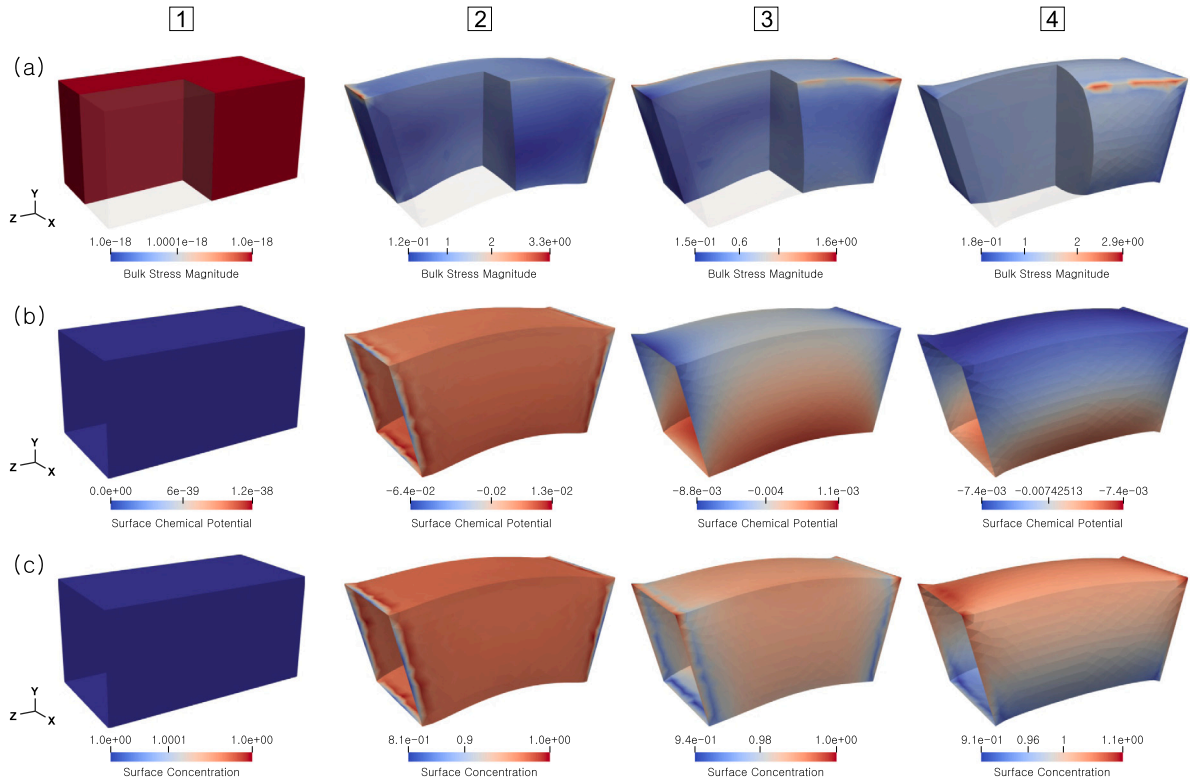

Fig. 6. Temporal sequence of (a) bulk stress, (b) surface chemical potential, and (c) surface concentration during the bending of a beam, with all variables normalized. The images are captured at normalized times $t/\tau = 0.0$, 0.01, 2.0, and 1.9×10^6 from left to right, labeled as Step 1, 2, 3, and 4, respectively.

To further investigate the heterogeneous concentration distribution during uniaxial tension, four representative surface concentration profiles are plotted at $t/\tau = 0.0$, 1.0, 2.0, and 1.9×10^6 with respect to the referential positions for comparison (Fig. 5). Initially, the surface concentration is uniformly set to unity. During the uniaxial tension process, the surface concentration increases at the clamped ends ($Z = 0$ and $Z = 2$) while decreasing in the interior. This trend persists until the equilibrium state. Interestingly, the positions of maximum concentration are not located exactly at the ends, but are slightly shifted ($Z \approx 0.1$ and $Z \approx 1.9$). Additionally, the positions of minimum concentration are not at the center ($Z = 1$), but are instead slightly shifted away from the center ($Z \approx 0.82$ and $Z \approx 1.18$). Note that the solution should theoretically be symmetric at $Z = 1$ due to the symmetric geometry; however, small perturbations, such as finite element mesh distortions, may affect the numerical process, leading to slight asymmetries in the solution.

5.2. Bending of a soft beam

In this example, we explore the non-equilibrium responses under bending conditions. The edge length of the cross-section is set as H, and the length of the bar is $2H$. Initially, the cylinder and film are stress-free, and the body force is ignored. Unlike the previous example in Section 5.1 where we focused on stretching, here we probe a more complex scenario involving bending. For the boundary conditions, we linearly ramp the displacement boundary condition from zero to its prescribed value within the time interval $t/\tau \in [0.0, 0.01]$. During this interval, both ends of the beam gradually rotate up to 26.56 degree around the center-line, resulting in the upper part of the beam being stretched and the lower part being compressed.

In Fig. 6, we showcase the temporal evolution of the finite element simulation for bulk stress, surface chemical potential, and surface concentration, with all values normalized. To focus on the contour plot on two sections of the interior along with the field on the exterior, we have removed a quarter of the domain from the images of bulk stresses in Fig. 6(a). The images are captured at normalized times $t/\tau = 0.0$, 0.01, 2.0, and 1.9×10^6 from left to right, labeled as Step 1, 2, 3, and 4, respectively. In Step 1 of Fig. 6, the beams represent the initial states, where the initial conditions remain the same as in the previous example (Section 5.1). Step 2 of Fig. 6 corresponds to the time step where the boundary conditions are linearly ramped up to a 26.56 degree rotation. As the beam bends, bulk stresses increase, particularly at the sharp

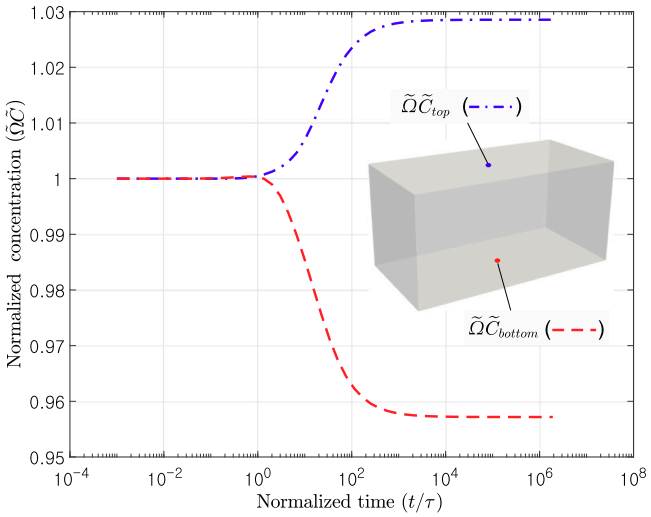

Fig. 7. Normalized surface concentrations ($\widetilde{\Omega C}$) at top and bottom points tracked over normalized time (t/τ). During the bending of the beam ($t/\tau < 0.01$), the surface concentrations at the top and bottom are nearly the same. However, as the bending progresses, the surface concentration at the top (under tension) increases, while the one at the bottom (under compression) decreases.

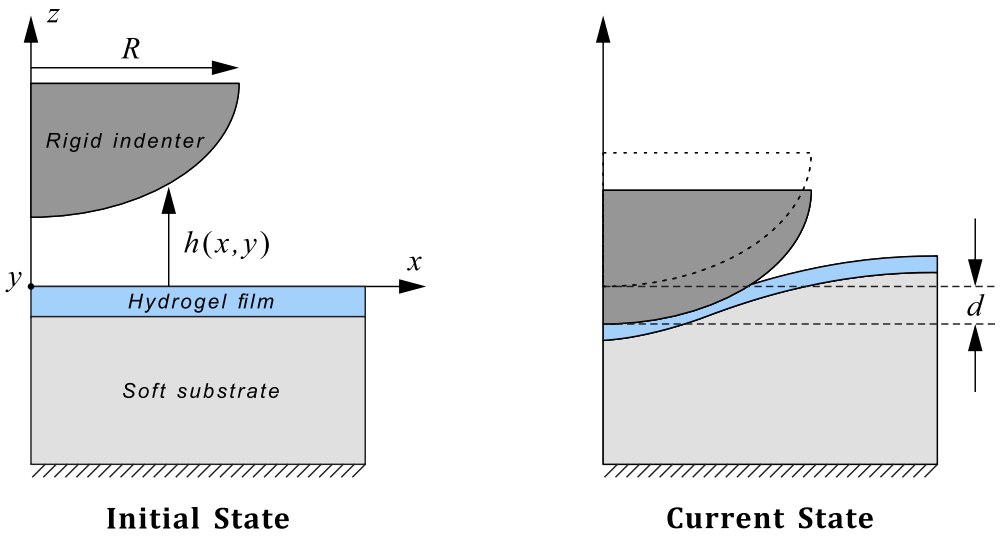

Fig. 8. Schematic illustration of the initial and current states of indentation-induced deformation and diffusion in a film-coated soft block. In the initial state, the rigid indenter has a radius R, and its surface is described by $h(x, y)$. In the current state, the rigid indenter pushes the block to a depth of d, resulting in surface diffusion and substrate deformation.

edges and corners. The surface chemical potential and concentration decrease, but some boundary effects near both ends are observable.

Beyond Step 2, for the remainder of the transient response, the boundary condition is held fixed, and we exponentially increase the time steps toward equilibrium. Throughout the transient analysis, our focus is on observing non-equilibrium responses and their multiphysical complexities. In Step 3, the beam continues to deform beyond the fixed boundary condition, representing the viscoelastic response. While observing the relaxation of bulk stress, we interestingly note stress concentration at the corners (Fig. 6(a), Step 3). This relaxation leads to the heterogeneous surface chemical potential of the film (Fig. 6(c), Step 3) and results in heterogeneous surface concentration (Fig. 6(b), Step 3). The non-equilibrium processes persist, and the system reaches the equilibrium state at Step 4. The boundary effect disappears, and we observe an increase in surface concentration in the upper stretched part and a decrease in the lower compressed part. We plot the surface concentration at the top and bottom surfaces, corresponding to the stretched and compressed regions, respectively (Fig. 7). Interestingly, the concentrations remain almost the same until $t/\tau \approx 1$, even though the beam is completely bent. However, as the non-equilibrium processes continue, the surface concentration at the top surface increases, and the surface concentration at the bottom surface decreases. This observation emphasizes the impact of the viscoelastic response on surface diffusion.

5.3. Rigid sphere indentation of a film/substrate rectangular block

The indentation test is particularly important for characterizing the mechanical properties of soft films (Kolesnikov and Shatvorov, 2022; Che et al., 2024), a critical aspect of advanced mechanical design, such as in the development of nano-indentation test techniques of identifying the constitutive parameters for soft tissue and membrane (Deuschle et al., 2007; Giolando et al., 2023), the development of high-performance semiconductor packaging (Tsui and Pharr, 1999; Sharma et al., 2022) and the development of robotic skin and sensor (Park et al., 2022; Hegde et al., 2023). However, there is limited understanding of the effect of surface diffusion and substrate viscoelasticity between the film/substrate system and the indenter, which can significantly impact the accurate characterization of material properties in thin soft films. Motivated by these observations, this study explores the transient response to indentation, highlighting both viscoelastic and poroelastic relaxation phenomena. The top and bottom dimensions (x-y plane dimension) are set as an edge length of H, and the height is $H/2$.

Regarding boundary conditions, the bottom surface is clamped, and the remaining surfaces are stress-free, and the body force is ignored. Notably, the indenter is not explicitly modeled, but we only consider the surface of the rigid indenter as follows.

$$h(x, y) = h_0 + \frac{1}{2R}\left(x^2 + y^2\right) \tag{5.1}$$

where h_0 is the initial gap between the top surface and the tip of the rigid indenter. If $h > 0$, there is no contact between both surfaces; contact appears only if $h \leq 0$. We linearly ramp the rigid indentation from zero to its maximum depth $d = 0.1H$ within the time interval $t/\tau \in [0.0, 0.01]$, where the radius of the rigid indenter is $R = 0.2H$ (Fig. 8). To facilitate this, we use the contact formation with penalty approach, which leads to the pressure p on the contact surface:

$$p = k_p\langle -g\rangle \quad \text{where} \quad g = h - u_z \tag{5.2}$$

where $\langle x\rangle = (|x| + x)/2$ is the Macaulay brackets, k_p is the penalty coefficient, g is the gap, and u_z is the displacement in the direction z. The weak form to account for the contact problem of rigid indentation can be formulated as:

$$\begin{aligned}
&\int_V \widehat{\mathbf{P}} : \boldsymbol{\nabla}_{\widehat{\mathbf{X}}}\delta\widehat{\mathbf{u}}\,\mathrm{d}\widehat{V} + \int_S \widehat{\widetilde{\mathbf{P}}} : \widetilde{\boldsymbol{\nabla}}_{\widehat{\mathbf{X}}}\delta\widehat{\mathbf{u}}\,\mathrm{d}\widehat{S} \\
&+ \int_S \left(\widehat{\widetilde{C}} - \widehat{\widetilde{C}}^{\,i}\right)\delta\widehat{\widetilde{\mu}}\,\mathrm{d}\widehat{S} + \Delta\widehat{t}\int_S \left(\widehat{\widetilde{C}}\widetilde{\mathbf{C}}^{-1}\cdot\widehat{\widetilde{\boldsymbol{\nabla}}}_{\widehat{\mathbf{X}}}\widehat{\widetilde{\mu}}\right)\cdot\widehat{\widetilde{\boldsymbol{\nabla}}}_{\widehat{\mathbf{X}}}\delta\widehat{\widetilde{\mu}}\,\mathrm{d}\widehat{S} \\
&+ \widehat{k}_p\int_{S_{top}} \langle\widehat{u}_z - \widehat{h}\rangle\delta\widehat{u}_z\,\mathrm{d}\widehat{S} = 0
\end{aligned} \tag{5.3}$$

The last term on left-hand side in Eq. (5.3) is the penalty formulation for contact problem (Belytschko et al., 2014; Bleyer, 2018), where S_{top} denotes the top surface of the rectangular block, and the weak form is normalized with respect to the characteristic length scale H. The normalized penalty coefficient is set as $\widehat{k}_p = 100$, which is sufficiently larger than the material moduli.

In Fig. 9, we showcase the temporal evolution of the finite element simulation for surface chemical potential, concentration and flux, with all values normalized. The images are captured at normalized times $t/\tau = 0.0$, 0.01, 2.0, and 1.9×10^6 from left to right, labeled as Step 1, 2, 3, and 4, respectively. In Step 1 of Fig. 9, the block represent the initial state, where the initial conditions remain the same as in the previous examples (Section 5.1). Step 2 of Fig. 9 corresponds to the time step where rigid indentation reach the prescribed depth. As the indenter punch the block, surface chemical potential decreases (Fig. 9a), which leads to the surface flux into the indented (or contacted) region (Fig.

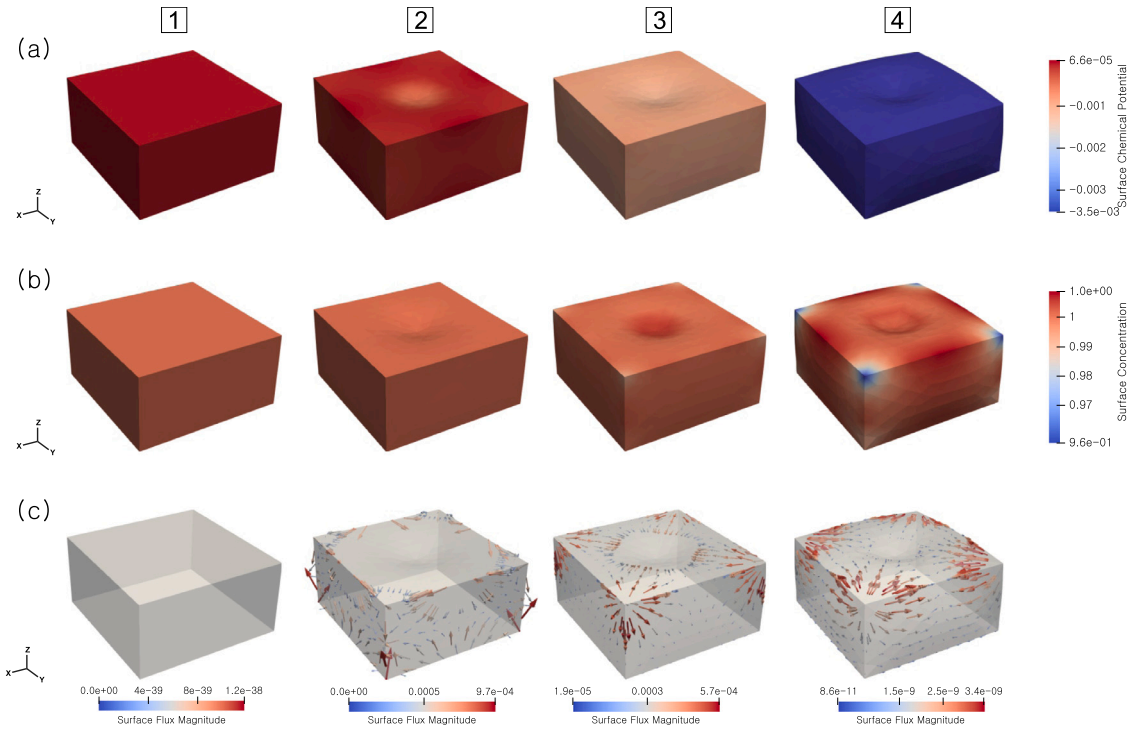

Fig. 9. Temporal sequence of (a) surface chemical potential, (b) surface concentration, and (c) surface flux during the indentation, with all variables normalized. The images are captured at normalized times $t/\tau = 0.0$, 0.01, 2.0, and 1.9×10^6 from left to right, labeled as Step 1, 2, 3, and 4, respectively.

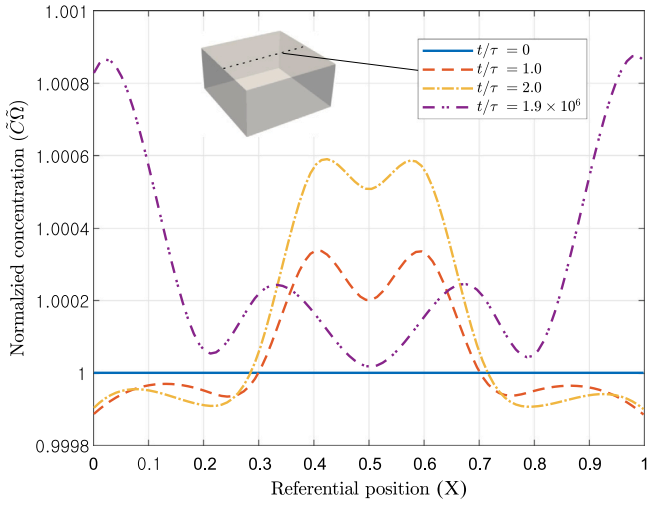

Fig. 10. Surface concentration profile during rigid sphere indentation. Normalized surface concentrations ($\widetilde{\Omega}\widetilde{C}$) are tracked over normalized time (t/τ). Four representative profiles are shown at $t/\tau = 0.0$, 1.0, 2.0, and 1.9×10^6. The surface concentrations are measured at reference positions along the centerline on the top surface of the rectangular block. Note that the radius of the rigid indenter is 0.2, but the radius of the actual contact area is smaller than 0.2 (Fig. 8).

9c). Beyond Step 2, for the remainder of the transient response, the indentation depth is held fixed, with the rigid indenter kept in position, and we exponentially increase the magnitude of the time steps toward equilibrium. In Step 3, the block continues to deform, representing the viscoelastic response. The system reaches the equilibrium state at Step 4, where there is heterogeneous surface concentration and deformed substrate.

To further investigate the heterogeneous concentration distribution during indentation, four representative surface concentration profiles were plotted at $t/\tau = 0.0$, 1.0, 2.0, and 1.9×10^6 with respect to the reference positions (Fig. 10). Initially, the surface concentration is uniformly set to unity. During the indentation process, the surface concentration increases near the contact area (from $X \approx 0.3$ to $X \approx 0.7$) while decreasing in the outer regions (from $X \approx 0.0$ to $X \approx 0.3$ and from $X \approx 0.7$ to $X \approx 1.0$). Interestingly, at equilibrium ($t/\tau = 1.9 \times 10^6$), this trend is reversed. Notably, the maximum concentration positions are not near the contact area but rather at the corners ($X \approx 0.05$ and $X \approx 1.95$), while the minimum concentration occurs at the center ($X = 0.5$). This observation suggests that while species accumulate in the contact region during indentation, they flow out due to substrate relaxation. Additionally, it is noteworthy that the total amount of species on the top surface increases during both indentation and relaxation, indicating that species migrate from the side surfaces to the top surface.

6. Discussion

A comprehensive multiphysics model, integrating surface diffusion, surface elasticity and bulk viscoelasticity, has been introduced and implemented using finite element analysis. The governing equations for non-equilibrium processes in a continuum body are established for surface poroelasticity and bulk viscoelasticity, with constitutive relations derived in a thermodynamically-consistent manner. This formulation is specialized for a hydrogel film and impermeable viscoelastic soft substrate. The numerical solution, is based on a mixed finite element method and implemented using the open-source framework FEniCS.

In the first example, involving the stretching of a cylindrical bar (Figs. 3–5 in Section 5.1), evolution of internal variables, bulk and surface stresses, surface chemical potential, concentration, and surface flux are examined. Contrary to expectations, the results in Fig. 3(c) show that film stress does not relax similar to substrate stress relaxation but has an opposite trend, highlighting the significant role of multi-physical complexities in comprehending the responses of soft solids. The second example (Figs. 6 and 7 in Section 5.2) further investigates the bending of the beam to test the more complex scenarios, which reveals significant differences in the pathways of species migration.

This observation clarifies that the surface diffusion and substrate relaxation could be important in the species distribution on the film. In the third example (Section 5.3), we delve into the more practical scenario of indentation-driven deformation and diffusion, considering the widespread use of hydrogel films in engineering applications such as sensors, drug delivery systems, and biomedical engineering. In this numerical study (Figs. 9 and 10), we reveal that in the early stages, the solvent within the film flows into the indented region, while the substrate deformation is concentrated primarily within the contact area. As the transient process progresses, the solvent migrates toward the corners of the substrate, causing deformation outside the initial contact region. This observation provides crucial insights into the indentation testing used to characterize the mechanical properties of hydrogel-based films. For example, the proposed methods could be employed to better interpret load–displacement curves in indentation tests, offering an alternative to the classical Hertzian solution.

The presented studies were not without their limitations. First, the proposed model does not account for variations in film thickness. In this research, we adopt the incompressibility condition, which indicate the species concentration is deterministic with respect to the substrate deformation. In the future work, one may solve the three-field weak form of three independent variables (displacement, chemical potential, and species concentration) for more general simulation (Kaessmair and Steinmann, 2016; Kaessmair et al., 2021). Second, this study assumes incompressibility of the molecular species and film networks, ignoring any potential void spaces. In reality, films may contain void spaces and exhibit some compressibility, which could affect their behavior. Third, this study does not explore the differing time scales of surface diffusion and substrate viscoelasticity. While it would be interesting to investigate how these distinct non-equilibrium processes compete during transient responses, this study assumes that the time scales are identical, focusing primarily on the heterogeneous surface concentration in response to substrate deformation. Fourth, the numerical tests have not been validated with experimental data. The material properties and time scales were selected for convenience in finite element simulations, rather than being based on experimental measurements. To alleviate this limitation and provide mechanical insights through the numerical tests, the finite element simulations were conducted using normalized material properties.

Although this study has some limitations, it still provides valuable insights into the behavior of 3D film/substrate systems. Notably, the continuum mechanics formulation presented for these systems is non-trivial, given the non-matching initial and stress-free reference states of the film and substrate. A key finding is the significant impact of multiphysical processes and their intricate coupling, suggesting that surface diffusion could be an important design factor in advanced manufacturing processes, particularly for films with porous properties. For example, in the uniaxial tension test discussed in Section 5.1, one might expect the species concentration to be lowest at the center of the bar due to symmetry. However, the results deviate from this expectation (Fig. 5), highlighting the complexity of film/substrate interactions and the necessity for advanced theoretical and computational frameworks. Additionally, the variation in surface concentration could significantly affect the outcomes of indentation tests. As demonstrated in the numerical indentation test (Figs. 10), surface concentration changes during the indentation and relaxation processes, underscoring the need to account for species concentration when aiming for more accurate and efficient measurements of the mechanical properties of thin films. These findings could be leveraged in the design of soft material-based engineering components.

7. Conclusion

In this paper, we investigated the time-dependent response of a porous film on a viscoelastic substrate. The governing equations were derived in a thermodynamically consistent manner, based on nonlinear poroelastic theory, incorporating surface kinematics to eliminate the need for 3D meshing of the film, instead utilizing a 2D mesh embedded on the substrate. Three loading conditions were considered, and our findings highlight the intricate interplay between competing multiphysical processes. These results provide a robust theoretical and computational mechanics framework for investigating the effects of mass transport on viscoelastic substrates.

For future work, it would be interesting to extend our model to include surface instability mechanisms, such as wrinkling, which could significantly enhance or suppress surface diffusion in a controlled, patterned manner. Additionally, applying the indentation test from Section 5.3 to estimate the mechanical properties of thin films with cross-validation against experimental data, where surface diffusion and substrate relaxation are non-negligible, represent an interesting direction to pursue.

CRediT authorship contribution statement

Seung-Hwan Boo: Writing – review & editing. **Jaemin Kim:** Writing – review & editing, Writing – original draft, Visualization, Validation, Supervision, Software, Resources, Project administration, Methodology, Investigation, Funding acquisition, Formal analysis, Data curation, Conceptualization.

Declaration of competing interest

The authors declare the following financial interests/personal relationships which may be considered as potential competing interests: Jaemin Kim reports financial support was provided by Changwon National University. If there are other authors, they declare that they have no known competing financial interests or personal relationships that could have appeared to influence the work reported in this paper.

Acknowledgments

Jaemin Kim: This research was funded by the 'New Faculty Research Support Grant' at Changwon National University in 2025. **Seung-HwanBoo**: This work was supported by the Ministry of Trade, Industry and Energy (MOTIE), Korea, under the Shipbuilding and Marine Engineering Technology Development Program (RS-2024-00460088). The authors thank Dr. Nikolaos Bouklas and Dr. Keon Ho Kim for discussion regarding the theoretical and mathematical formulation.

Appendix A. Derivation of surface stress and algebraic equation for free swelling stretch

In Fig. A.11, the homogeneously swollen stress-free (initial) state can be described using the initial stretch ratio $\widetilde{\lambda}_0$ and the corresponding deformation gradient $\widetilde{\mathbf{F}}_0 = \widetilde{\lambda}_0\widetilde{\mathbf{I}}$, with the corresponding surface Jacobian determinant given by $\widetilde{J}_0 = \widetilde{\lambda}_0^2$. The deformation of the film on the substrate can be described using surface kinematics denoted by $\widetilde{\mathbf{F}}$ (Fig. 1). As the solvent concentration $\widetilde{C}$ is defined with respect to the initial (swollen) state, and the solvent concentration with respect to the dry state is given by $\widetilde{J}_0\widetilde{C}$.

By performing a Legendre transform, the surface strain energy density at the initial (swollen) state can be written as:

$$\widetilde{\Psi}(\widetilde{\mathbf{F}},\widetilde{\mu}) = \frac{1}{2}\frac{\widetilde{G}}{\widetilde{J}_0}\left[\widetilde{\lambda}_0^2\,\widetilde{I}_1 - 2 - 2\ln\left(\widetilde{J}_0\widetilde{J}\right)\right] - \widetilde{\mu}\widetilde{C} - \frac{\widetilde{\beta}}{\widetilde{J}_0}\frac{k_B T}{\widetilde{\Omega}}\left[\widetilde{\Omega}\widetilde{J}_0\widetilde{C}\ln\left(\frac{1+\widetilde{\Omega}\widetilde{J}_0\widetilde{C}}{\widetilde{\Omega}\widetilde{J}_0\widetilde{C}}\right) + \frac{\widetilde{\chi}}{1+\widetilde{\Omega}\widetilde{J}_0\widetilde{C}}\right] \tag{A.1}$$

The surface first Piola–Kirchhoff stress can be derived by constitutive relation of Eq. (3.8),

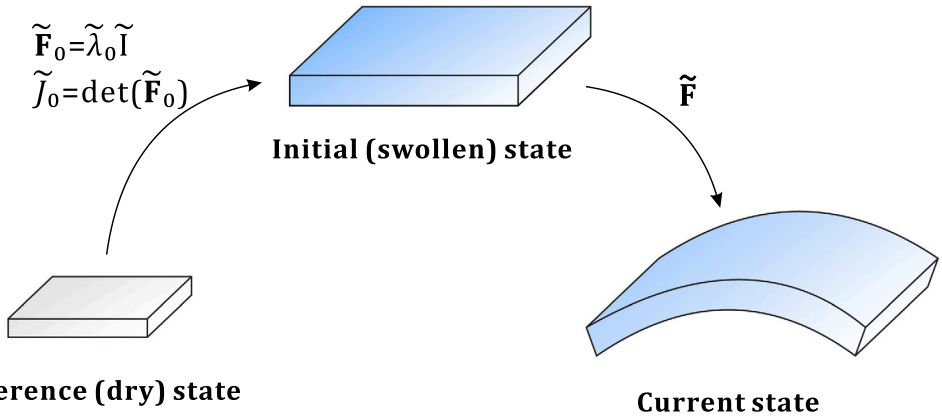

Fig. A.11. Schematic illustration of the dry, swollen (initial), and current states of a hydrogel film. The initial state represents the free-swollen hydrogel given the initial chemical potential $\widetilde{\mu}_0$, isotropically scaled from the reference state. The stretch and the Jacobian determinant are denoted as $\widetilde{\lambda}_0$ and $\widetilde{J}_0$. The swollen hydrogel is attached to the substrate that is assumed to be initial state (also Fig. 1), and its current state is characterized by the surface deformation gradient $\widetilde{\mathbf{F}}$.

$$\widetilde{\mathbf{P}}(\widetilde{\mathbf{F}},\widetilde{\mu}) = \frac{\widetilde{G}}{\widetilde{J}_0}\left(\widetilde{\lambda}_0^2\widetilde{\mathbf{F}} - \widetilde{\mathbf{F}}^{-\mathrm{T}}\right) - \frac{\widetilde{\mu}}{\widetilde{\Omega}}\widetilde{J}\widetilde{\mathbf{F}}^{-\mathrm{T}} + \frac{\widetilde{\beta}}{\widetilde{J}_0}\frac{k_B T}{\widetilde{\Omega}}\left[\widetilde{J}_0\ln\left(1-\frac{1}{\widetilde{J}_0\widetilde{J}}\right)+\frac{1}{\widetilde{J}}+\frac{\widetilde{\chi}}{\widetilde{J}_0\widetilde{J}^2}\right]\widetilde{J}\widetilde{\mathbf{F}}^{-\mathrm{T}} \tag{A.2}$$

which corresponds to Eq. (3.10) in manuscript. The initial conditions for hydrogel film at free swollen state are given by:

$$\widetilde{J}_0 = \widetilde{\lambda}_0^2, \quad \widetilde{\mu} = \widetilde{\mu}_0, \quad \widetilde{\mathbf{F}} = \widetilde{\mathbf{I}}, \quad \widetilde{J} = 1 \tag{A.3}$$

By substituting Eq. (A.3) into Eq. (A.2), the surface first Piola–Kirchhoff stress at the initial (free swollen) state can be obtained,

$$\frac{1}{\widetilde{G}}\widetilde{\mathbf{P}}(\widetilde{\lambda}_0,\widetilde{\mu}_0) = \left(1-\frac{1}{\widetilde{\lambda}_0^2}+\frac{\widetilde{\beta}}{\widetilde{N}\widetilde{\Omega}}\left[\ln\left(1-\frac{1}{\widetilde{\lambda}_0^2}\right)+\frac{1}{\widetilde{\lambda}_0^2}+\frac{\widetilde{\chi}}{\widetilde{\lambda}_0^4}-\frac{\widetilde{\lambda}_0^2}{\widetilde{\beta}}\frac{\widetilde{\mu}_0}{k_B T}\right]\right)\widetilde{\mathbf{I}} = \mathbf{O} \tag{A.4}$$

Finally we can obtain the non-linear algebraic equation,

$$1-\frac{1}{\widetilde{\lambda}_0^2}+\frac{\widetilde{\beta}}{\widetilde{N}\widetilde{\Omega}}\left[\ln\left(1-\frac{1}{\widetilde{\lambda}_0^2}\right)+\frac{1}{\widetilde{\lambda}_0^2}+\frac{\widetilde{\chi}}{\widetilde{\lambda}_0^4}-\frac{\widetilde{\lambda}_0^2}{\widetilde{\beta}}\frac{\widetilde{\mu}_0}{k_B T}\right] = 0 \tag{A.5}$$

where the equation determines the initial stretch (free swelling ratio) $\widetilde{\lambda}_0$ based on the initial chemical potential $\widetilde{\mu}_0$. In this study, we set $\widetilde{\mu}_0 = 0$ (fully swollen), $\widetilde{N}\widetilde{\Omega}/\widetilde{\beta} = 10^{-3}$, and $\widetilde{\chi} = 0.7705$, resulting in an initial stretch $\widetilde{\lambda}_0 \approx 1.42$. By the incompressibility condition (Eq. (3.5)), we find the initial solvent concentration, as $\widehat{\widetilde{C}}_0 \approx 1.0$.

Appendix B. Alternative weak formulation

In the manuscript, the weak forms were derived with respect to displacement and chemical potential through the Legendre transformation. This approach was adopted for two main reasons: it simplifies the application of chemical boundary conditions, and it avoids the need for C^1 continuity in numerical modeling. In this appendix, we provide an alternative weak formulation with respect to the species concentration (instead of chemical potential), which does not employ Legendre transformation.

Starting from Eq. (2.13), we multiply it by the test function $\delta\widetilde{C}$ and integrate over the domain. This results in:

$$\int_S \hat{\widetilde{C}}\,\delta\widetilde{C}\,\mathrm{d}S - \int_S \widetilde{\boldsymbol{\nabla}}_{\widetilde{\mathbf{X}}}\cdot\widetilde{\mathbf{J}}\,\delta\widetilde{C}\,\mathrm{d}S = 0 \tag{B.1}$$

Substituting Eq. (2.23) for the flux $\widetilde{\mathbf{J}}$ into Eq. (B.1), we obtain:

$$\int_S \hat{\widetilde{C}}\,\delta\widetilde{C}\,\mathrm{d}S + \int_S \widetilde{\boldsymbol{\nabla}}_{\widetilde{\mathbf{X}}}\cdot\left(\widetilde{\mathbf{M}}\cdot\widetilde{\boldsymbol{\nabla}}_{\widetilde{\mathbf{X}}}\widetilde{\mu}\right)\delta\widetilde{C}\,\mathrm{d}S = 0 \tag{B.2}$$

Here, $\widetilde{\mu}$ is determined by the constitutive relation in Eq. (2.22). It is critical to note that $\widetilde{\mu}$ involves a second derivative with respect to $\widetilde{\mathbf{X}}$. Consequently, the weak formulation requires C^1 continuity for numerical implementation (i.e., at least second-order differentiability of the variables), whereas standard finite element methods employ C^0 continuity.

Data availability

Data will be made available on request.

References

Alnæs, Martin S., Blechta, Jan, Hake, Johan, Johansson, August, Kehlet, Benjamin, Logg, Anders, Richardson, Chris, Ring, Johannes, Rognes, Marie E., Wells, Garth N., 2015. The FEniCS project version 1.5. Arch. Numer. Softw. 3 (100).

Ang, Ida, Liu, Zezhou, Kim, Jaemin, Hui, Chung-Yuen, Bouklas, Nikolaos, 2020. Effect of elastocapillarity on the swelling kinetics of hydrogels. J. Mech. Phys. Solids 104132.

Askari-Sedeh, Mahdi, Baghani, Mostafa, 2023. Coupled chemo-mechanical swelling behavior of ph-sensitive hollow cylinder hydrogels under extension–torsion and internal pressure: Analytical and 3D FEM solutions. Int. J. Appl. Mech. 15 (04), 2350030.

Babuška, Ivo, 1971. Error-bounds for finite element method. Numer. Math. 16 (4), 322–333.

Baker, Brendon M, Trappmann, Britta, Wang, William Y, Sakar, Mahmut S, Kim, Iris L, Shenoy, Vivek B, Burdick, Jason A, Chen, Christopher S, 2015. Cell-mediated fibre recruitment drives extracellular matrix mechanosensing in engineered fibrillar microenvironments. Nat. Mater. 14 (12), 1262–1268.

Balay, Satish, Abhyankar, Shrirang, Adams, Mark, Brown, Jed, Brune, Peter, Buschelman, Kris, Dalcin, Lisandro, Dener, Alp, Eijkhout, Victor, Gropp, W, et al., 2019. PETSc Users Manual. Argonne National Laboratory.

Ballarin, F., 2019. Multiphenics – easy prototyping of multiphysics problems in FEniCS.

Bathe, Klaus-Jürgen, 2001. The inf–sup condition and its evaluation for mixed finite element methods. Comput. Struct. 79 (2), 243–252.

Belytschko, Ted, Liu, Wing Kam, Moran, Brian, Elkhodary, Khalil, 2014. Nonlinear Finite Elements for Continua and Structures. John wiley & sons.

Björklund, Martin, Larsson, Karl, Larson, Mats G., 2024. Error estimates for finite element approximations of viscoelastic dynamics: The generalized maxwell model. Comput. Methods Appl. Mech. Engrg. 425, 116933.

Bleyer, Jeremy, 2018. Numerical tours of computational mechanics with fenics. Zenodo.

Brezzi, Franco, 1974. On the existence, uniqueness and approximation of saddle-point problems arising from Lagrangian multipliers. Publ. Mathématiques et Inform. de Rennes (S4), 1–26.

Che, Haoyuan, Amar, Martine Ben, Zhu, Wei, Fan, Shengjun, Leng, Jinsong, Jia, Fei, Liu, Yanju, 2024. An indentation method to determine the constitutive parameters of hyperelastic films under large deformation: Theoretical model, experiments and simulations. Int. J. Solids Struct. 113007.

Chen, Jing, Wang, Dong, Wang, Long-Hai, Liu, Wanjun, Chiu, Alan, Shariati, Kaavian, Liu, Qingsheng, Wang, Xi, Zhong, Zhe, Webb, James, et al., 2020. An adhesive hydrogel with "load-sharing" effect as tissue bandages for drug and cell delivery. Adv. Mater. 32 (43), 2001628.

Cheng, Shing-Yi, Heilman, Steven, Wasserman, Max, Archer, Shivaun, Shuler, Michael L, Wu, Mingming, 2007. A hydrogel-based microfluidic device for the studies of directed cell migration. Lab A Chip 7 (6), 763–769.
Chester, Shawn A., Anand, Lallit, 2010. A coupled theory of fluid permeation and large deformations for elastomeric materials. J. Mech. Phys. Solids 58 (11), 1879–1906.
Chester, Shawn A., Di Leo, Claudio V., Anand, Lallit, 2015. A finite element implementation of a coupled diffusion-deformation theory for elastomeric gels. Int. J. Solids Struct. 52, 1–18.
Delavoipière, Jessica, Heurtefeu, Bertrand, Teisseire, Jérémie, Chateauminois, Antoine, Tran, Yvette, Fermigier, Marc, Verneuil, Emilie, 2018. Swelling dynamics of surface-attached hydrogel thin films in vapor flows. Langmuir 34 (50), 15238–15244.
Deuschle, Julia, Enders, Susan, Arzt, Eduard, 2007. Surface detection in nanoindentation of soft polymers. J. Mater. Res. 22 (11), 3107–3119.
Do Carmo, Manfredo P., 2016. Differential Geometry of Curves and Surfaces: Revised and Updated Second Edition. Courier Dover Publications.
Dortdivanlioglu, Berkin, Javili, Ali, 2021. Boundary viscoelasticity theory at finite deformations and computational implementation using isogeometric analysis. Comput. Methods Appl. Mech. Engrg. 374, 113579.
Drelich, Jaroslaw, Chibowski, Emil, Meng, Dennis Desheng, Terpilowski, Konrad, 2011. Hydrophilic and superhydrophilic surfaces and materials. Soft Matter 7 (21), 9804–9828.
Flory, P.J., 1961. Thermodynamic relations for high elastic materials. Trans. Faraday Soc. 57, 829–838.
Flory, Paul J., Rehner Jr., John, 1943. Statistical mechanics of cross-linked polymer networks II. Swelling. J. Chem. Phys. 11 (11), 521–526.
Fu, Xie, Tong, Hui, Zhang, Xia, Zhang, Kun, Douadji, Lyes, Kang, Shuai, Luo, Jinling, Pan, Ziwei, Lu, Wenqiang, 2023. Anisotropic hydrogels with multiscale hierarchy based on ionic conductivity for flexible sensors. ACS Appl. Polym. Mater..
Giolando, Patrick, Kakaletsis, Sotirios, Zhang, Xuesong, Weickenmeier, Johannes, Castillo, Edward, Dortdivanlioglu, Berkin, Rausch, Manuel K, 2023. AI-dente: an open machine learning based tool to interpret nano-indentation data of soft tissues and materials. Soft Matter 19 (35), 6710–6720.
Goodbrake, C., Steigmann, D.J., 2018. Mechanics of an elastic membrane infused with a liquid. Int. J. Mech. Sci. 149, 487–493.
Green, Albert Edward, Zerna, Wolfgang, 1992. Theoretical Elasticity. Courier Corporation.
Gurtin, Morton E., Fried, Eliot, Anand, Lallit, 2010. The Mechanics and Thermodynamics of Continua. Cambridge University Press.
Hall, Matthew S, Alisafaei, Farid, Ban, Ehsan, Feng, Xinzeng, Hui, Chung-Yuen, Shenoy, Vivek B, Wu, Mingming, 2016. Fibrous nonlinear elasticity enables positive mechanical feedback between cells and ECMs. Proc. Natl. Acad. Sci. 113 (49), 14043–14048.
Hegde, Chidanand, Su, Jiangtao, Tan, Joel Ming Rui, He, Ke, Chen, Xiaodong, Magdassi, Shlomo, 2023. Sensing in soft robotics. ACS Nano 17 (16), 15277–15307.
Holzapfel, Gerhard A., 2002. Nonlinear solid mechanics: a continuum approach for engineering science.
Hong, Wei, Liu, Zishun, Suo, Zhigang, 2009. Inhomogeneous swelling of a gel in equilibrium with a solvent and mechanical load. Int. J. Solids Struct. 46 (17), 3282–3289.
Hong, Wei, Zhao, Xuanhe, Zhou, Jinxiong, Suo, Zhigang, 2008. A theory of coupled diffusion and large deformation in polymeric gels. J. Mech. Phys. Solids 56 (5), 1779–1793.
Hu, Lixuan, Chee, Pei Lin, Sugiarto, Sigit, Yu, Yong, Shi, Chuanqian, Yan, Ren, Yao, Zhuoqi, Shi, Xuewen, Zhi, Jiacai, Kai, Dan, et al., 2023. Hydrogel-based flexible electronics. Adv. Mater. 35 (14), 2205326.
Hughes, Thomas J.R., 2012. The Finite Element Method: Linear Static and Dynamic Finite Element Analysis. Courier Corporation.
Huo, Ni, Ye, Sheng, Ouderkirk, Andrew J., Tenhaeff, Wyatt E., 2022. Porous polymer films with tunable pore size and morphology by vapor deposition. ACS Appl. Polym. Mater. 4 (10), 7300–7310.
Javili, Ali, Steinmann, Paul, 2009. A finite element framework for continua with boundary energies. Part I: the two-dimensional case. Comput. Methods Appl. Mech. Engrg. 198 (27–29), 2198–2208.
Javili, A., Steinmann, Paul, 2010. A finite element framework for continua with boundary energies. Part II: The three-dimensional case. Comput. Methods Appl. Mech. Engrg. 199 (9–12), 755–765.
Kaessmair, Stefan, Runesson, Kenneth, Steinmann, Paul, Jänicke, Ralf, Larsson, Fredrik, 2021. Variationally consistent computational homogenization of chemomechanical problems with stabilized weakly periodic boundary conditions. Internat. J. Numer. Methods Engrg. 122 (22), 6429–6454.
Kaessmair, Stefan, Steinmann, Paul, 2016. Comparative computational analysis of the Cahn–Hilliard equation with emphasis on c1-continuous methods. J. Comput. Phys. 322, 783–803.
Kim, Jaemin, Ang, Ida, Ballarin, Francesco, Hui, Chung-Yuen, Bouklas, Nikolaos, 2023b. A finite element implementation of finite deformation surface and bulk poroelasticity. Comput. Mech..
Kim, Jaemin, Mailand, Erik, Ang, Ida, Sakar, Mahmut Selman, Bouklas, Nikolaos, 2020. A model for 3D deformation and reconstruction of contractile microtissues. Soft Matter.
Kim, Jaemin, Mailand, Erik, Sakar, Mahmut Selman, Bouklas, Nikolaos, 2023a. A model for mechanosensitive cell migration in dynamically morphing soft tissues. Extrem. Mech. Lett. 58, 101926.
Kim, Jaemin, Sakar, Mahmut Selman, Bouklas, Nikolaos, 2024. Modeling the mechanosensitive collective migration of cells on the surface and the interior of morphing soft tissues. Biomech. Model. Mechanobiol. 1–21.
Kolesnikov, Alexey M., Shatvorov, Nikita M., 2022. Indentation of a circular hyperelastic membrane by a rigid cylinder. Int. J. Non-Linear Mech. 138, 103836.
Kopecek, Jindrich, 2009. Hydrogels: From soft contact lenses and implants to self-assembled nanomaterials. J. Polym. Sci. Part A: Polym. Chem. 47 (22), 5929–5946.
Li, Bo, Cao, Yan-Ping, Feng, Xi-Qiao, Gao, Huajian, 2012. Mechanics of morphological instabilities and surface wrinkling in soft materials: a review. Soft Matter 8 (21), 5728–5745.
Lin, Shaoting, Yuk, Hyunwoo, Zhang, Teng, Parada, German Alberto, Koo, Hyunwoo, Yu, Cunjiang, Zhao, Xuanhe, 2016. Stretchable hydrogel electronics and devices. Adv. Mater. 28 (22), 4497–4505.
Linder, Christian, Tkachuk, Mykola, Miehe, Christian, 2011. A micromechanically motivated diffusion-based transient network model and its incorporation into finite rubber viscoelasticity. J. Mech. Phys. Solids 59 (10), 2134–2156.
Liu, Rui-Cheng, Liu, Yang, Goriely, Alain, 2024. Surface wrinkling of a film coated to a graded substrate. J. Mech. Phys. Solids 186, 105603.
Liu, Wenlong, Wang, Hong, 2020. Flexible oxide epitaxial thin films for wearable electronics: Fabrication, physical properties, and applications. J. Mater. 6 (2), 385–396.
Liu, Yu, Ye, Hongfei, Zhang, Hongwu, Zheng, Yonggang, 2023. Coupling phase-field LB–MP method for multiphase fluid–deformable solid interaction problems involving large density and viscosity contrasts. Int. J. Appl. Mech. 15 (06), 2350050.
Logg, Anders, Mardal, Kent-Andre, Wells, Garth, 2012. Automated Solution of Differential Equations by the Finite Element Method: The FEniCS Book. vol. 84, Springer Science & Business Media.
Lucantonio, Alessandro, Nardinocchi, Paola, Teresi, Luciano, 2013. Transient analysis of swelling-induced large deformations in polymer gels. J. Mech. Phys. Solids 61 (1), 205–218.
Lucantonio, Alessandro, Teresi, Luciano, DeSimone, Antonio, 2016. Continuum theory of swelling material surfaces with applications to thermo-responsive gel membranes and surface mass transport. J. Mech. Phys. Solids 89, 96–109.
MacMinn, Christopher W., Dufresne, Eric R., Wettlaufer, John S., 2016. Large deformations of a soft porous material. Phys. Rev. Appl. 5 (4), 044020.
Mailand, Erik, Özelçi, Ece, Kim, Jaemin, Rüegg, Matthias, Chaliotis, Odysseas, Märki, Jon, Bouklas, Nikolaos, Sakar, Mahmut Selman, 2022. Tissue engineering with mechanically induced solid-fluid transitions. Adv. Mater. 34 (2), 2106149.
Martinez, Ramses V, Glavan, Ana C, Keplinger, Christoph, Oyetibo, Alexis I, Whitesides, George M, 2014. Soft actuators and robots that are resistant to mechanical damage. Adv. Funct. Mater. 24 (20), 3003–3010.
McBride, A.T., Javili, A., Steinmann, P., Bargmann, Swantje, 2011. Geometrically nonlinear continuum thermomechanics with surface energies coupled to diffusion. J. Mech. Phys. Solids 59 (10), 2116–2133.
Moreau, David, Chauvet, Caroline, Etienne, François, Rannou, François P, Corté, Laurent, 2016. Hydrogel films and coatings by swelling-induced gelation. Proc. Natl. Acad. Sci. 113 (47), 13295–13300.
Murad, Márcio A., Loula, Abimael F.D., 1994. On stability and convergence of finite element approximations of Biot's consolidation problem. Internat. J. Numer. Methods Engrg. 37 (4), 645–667.
Park, Kyungseo, Yuk, Hyunwoo, Yang, M, Cho, Junhwi, Lee, Hyosang, Kim, Jung, 2022. A biomimetic elastomeric robot skin using electrical impedance and acoustic tomography for tactile sensing. Sci. Robot. 7 (67), eabm7187.
Park, Byung-Wook, Zhuang, Jiang, Yasa, Oncay, Sitti, Metin, 2017. Multifunctional bacteria-driven microswimmers for targeted active drug delivery. ACS Nano 11 (9), 8910–8923.
Rasitha, TP, Krishna, Nanda Gopala, Anandkumar, B, Vanithakumari, SC, Philip, John, 2024. A comprehensive review on anticorrosive/antifouling superhydrophobic coatings: Fabrication, assessment, applications, challenges and future perspectives. Adv. Colloid Interface Sci. 103090.
Reinhart-King, Cynthia A., Dembo, Micah, Hammer, Daniel A., 2005. The dynamics and mechanics of endothelial cell spreading. Biophys. J. 89 (1), 676–689.
Rens, Elisabeth G., Merks, Roeland M.H., 2020. Cell shape and durotaxis explained from cell-extracellular matrix forces and focal adhesion dynamics. Iscience 23 (9).
Rossy, Tamara, Distler, Tania, Meirelles, Lucas A, Pezoldt, Joern, Kim, Jaemin, Talà, Lorenzo, Bouklas, Nikolaos, Deplancke, Bart, Persat, Alexandre, 2023. Pseudomonas aeruginosa type IV pili actively induce mucus contraction to form biofilms in tissue-engineered human airways. Plos Biology 21 (8), e3002209.
Sharma, Hemant Kumar, Sharma, Rajesh Kumar, Saxena, Raghvendra Sahai, Prasad, Rajesh, 2022. A review of nanoindentation and related cathodoluminescence studies on semiconductor materials. J. Mater. Sci., Mater. Electron. 33 (27), 21223–21245.
Song, Zhaoqiang, Li, Xu, Wu, Kaijin, Cai, Shengqiang, 2023. Nonequilibrium thermodynamic modeling of case II diffusion in glassy polymers. J. Mech. Phys. Solids 179, 105395.
Song, Zhaoqiang, Liang, Xiaodong, Li, Kai, Cai, Shengqiang, 2020. Surface mechanics of a stretched elastomer layer bonded on a rigid substrate. Int. J. Solids Struct. 200, 1–12.

Stamatialis, Dimitrios F, Papenburg, Bernke J, Gironés, Miriam, Saiful, Saiful, Bettahalli, Srivatsa NM, Schmitmeier, Stephanie, Wessling, Matthias, 2008. Medical applications of membranes: Drug delivery, artificial organs and tissue engineering. J. Membr. Sci. 308 (1–2), 1–34.

Steinmann, Paul, 2008. On boundary potential energies in deformational and configurational mechanics. J. Mech. Phys. Solids 56 (3), 772–800.

Steinmann, P., McBride, A.T., Bargmann, S., Javili, A., 2012. A deformational and configurational framework for geometrically non-linear continuum thermomechanics coupled to diffusion. Int. J. Non-Linear Mech. 47 (2), 215–227.

Taylor, Cedric, Hood, Paul, 1973. A numerical solution of the Navier-Stokes equations using the finite element technique. Comput. & Fluids 1 (1), 73–100.

Toomey, Ryan, Freidank, Daniel, Rühe, Jürgen, 2004. Swelling behavior of thin, surface-attached polymer networks. Macromolecules 37 (3), 882–887.

Tse, Justin R., Engler, Adam J., 2010. Preparation of hydrogel substrates with tunable mechanical properties. Curr. Protoc. Cell Biology 47 (1), 10–16.

Tsui, T.Y., Pharr, G.M., 1999. Substrate effects on nanoindentation mechanical property measurement of soft films on hard substrates. J. Mater. Res. 14 (1), 292–301.

Wallin, T.J., Pikul, James, Shepherd, Robert F., 2018. 3D printing of soft robotic systems. Nat. Rev. Mater. 3 (6), 84–100.

Wiener, Clinton G., Weiss, R.A., Vogt, Bryan D., 2014. Overcoming confinement limited swelling in hydrogel thin films using supramolecular interactions. Soft Matter 10 (35), 6705–6712.

Xu, Shuai, Liu, Zishun, 2020. Coupled theory for transient responses of conductive hydrogels with multi-stimuli. J. Mech. Phys. Solids 143, 104055.

Xu, Shuai, Liu, Zishun, 2023. A deformation–diffusion-coupled constitutive theory for hydrogels by considering the preparation conditions. Int. J. Appl. Mech. 15 (08), 2350062.

Xu, Qin, Wilen, Lawrence A, Jensen, Katharine E, Style, Robert W, Dufresne, Eric R, 2020. Viscoelastic and poroelastic relaxations of soft solid surfaces. Phys. Rev. Lett. 125 (23), 238002.

Xue, Yiheng, Liu, Zishun, Reddy, J.N., 2024. A three-fields coupled numerical framework for transient deformation of thermo-sensitive hydrogel. Internat. J. Numer. Methods Engrg. 125 (18), e7550.

Yang, Jiawei, Bai, Ruobing, Chen, Baohong, Suo, Zhigang, 2020. Hydrogel adhesion: a supramolecular synergy of chemistry, topology, and mechanics. Adv. Funct. Mater. 30 (2), 1901693.